Journal of Structural Geology 163 (2022) 104709

Contents lists available at ScienceDirect

Journal of Structural Geology

journal homepage: www.elsevier.com/locate/jsg

Strain localization at brittle-ductile transition depths during Miocene magmatism and exhumation in the southern Basin and Range

Andrew V. Zuza [a,*], Wenrong Cao [b], Angelica Rodriguez-Arriaga [a,b], Joel W. DesOrmeau [b], Margaret L. Odlum [c]

[a] Nevada Bureau of Mines and Geology, University of Nevada, Reno, NV, 89557, USA
[b] Department of Geological Sciences and Engineering, University of Nevada, Reno, NV, 89557, USA
[c] Department of Geoscience, University of Nevada, Las Vegas, NV, 89154, USA

ARTICLE INFO

Keywords:
Basin and Range
Brittle-ductile transition
Feldspar deformation
Deformation mechanism maps
Zircon helium thermochronology
EBSD

ABSTRACT

Feldspar dominates the middle and lower continental crust. Models of crustal rheology depend on our knowledge of feldspar deformation mechanisms. To learn more about natural feldspar deformation, we conducted a multidisciplinary investigation of a brittle-ductile transition (BDT) hosted within a Cretaceous pluton in the Colorado River Extensional Corridor, southern Nevada. Here, a distinct BDT was observed at ~10 km paleo-depth, where brittle faulting transitioned to discrete, localized ductile shearing. Field relationships confirm this BDT to have deformed and exhumed in the Miocene, temporally associated with the intrusion of two surrounding ca. 16 Ma plutons and subsequent footwall rotation in an east-directed normal-fault system. We established the overall structural framework, strain rates, and thermal histories through field traverses, aluminum-in-hornblende barometry to reconstruct paleo-depth, zircon (U–Th)/He thermochronology (ZHe) to constrain temperature-time histories, and 1D thermal models to further resolve deformation temperatures. Localized shear zones within the BDT formed ca. 16.2–15.5 Ma at temperatures of ~500–600 °C, which continued deforming as they cooled both conductively and advectively to ~200 °C by ca. 14 Ma, as constrained by ZHe dates. Strain was concentrated in fine-grained (7–10 μm) feldspar-rich ultramylonites that were interpreted to have primarily deformed via grain-size-sensitive diffusion creep. Grain-size reduction that allowed activation of diffusion creep likely resulted from brittle cataclasis, fluid-assisted fracturing and neocrystallization, and dislocation creep mechanisms, thus emphasizing the importance of these processes to localize deformation at relatively strong mid-crust conditions to facilitate the development of diffusion-creep shear zones. Grain-size piezometers suggest stresses of ~50 MPa, which are significantly weaker than peak strength in quartz-rich BDTs that deform via dislocation creep. This integrated process allows relatively low viscosities (~10^{18}–10^{19} Pa s) at lower crust temperatures and explains a coherent process of strain localization at near-BDT conditions in feldspar-dominated lithologies. We suggest that this naturally deformed feldspar shear zone was preserved due to the unique geologic history with fast heating and exhumation, which froze both brittle vs crystal-plastic structures to provide valuable insights into mechanisms of feldspar deformation.

1. Introduction

The thermal, temporal, and spatial evolution of the crustal brittle-ductile transition (BDT) is important for crustal strength, seismicity, and bulk lithosphere rheology (e.g., Burov, 2011; Kusznir and Park, 1984; Sibson, 1986, 1984; Sullivan et al., 2013; Zuza and Cao, 2020). This transition can be viewed from the perspective of experimental data and theory (Brace and Kohlstedt, 1980; Burov and Watts, 2006; Byerlee, 1968) or observed via present-day seismicity (Hauksson and Meier, 2019; Nazareth and Hauksson, 2004; Zuza and Cao, 2020). The best natural examples of BDTs come from extensional settings, which simultaneously deform upper-middle crustal rocks under relatively well constrained stress-temperature conditions and exhume the rocks to the surface to be directly observed in the field (Platt and Behr, 2011).

Quartz is one of the weaker bulk phases of the middle-upper continental crust, and most previous studies of exhumed shear zones—and

* Corresponding author.
E-mail addresses: azuza@unr.edu, avz5818@gmail.com (A.V. Zuza).

https://doi.org/10.1016/j.jsg.2022.104709
Received 29 March 2022; Received in revised form 1 July 2022; Accepted 19 August 2022
Available online 26 August 2022

specifically BDTs—focus on quartz deformation. However, feldspar is the most abundant mineral in the Earth's crust, and thus how it deforms has important implications for crustal rheology and continental tectonics (e.g., Bürgmann and Dresen, 2008; Rybacki and Dresen, 2004; Watts and Burov, 2003). Therefore, although quartz deformation may focus strain relative to feldspar in natural shear zones, how feldspar deforms is of critical importance for the bulk crust, polyphase deformation considerations (Platt, 2015), local regions where feldspar phases dominate, and/or in deformation conditions that promote strain weakening of feldspar (e.g., Sullivan et al., 2013; Tullis and Yund, 1987). Feldspar deformation mechanisms have been studied in both laboratory and natural field studies (e.g., Mehl and Hirth, 2008; Miranda et al., 2016; Olsen and Kohlstedt, 1984; Post and Tullis, 1999), focused on grain-size-insensitive dislocation creep (e.g., Cannat, 1991; Stünitz and Fitz Gerald, 1993; Kruse et al., 2001; Tullis and Yund, 1985), and grain-size-sensitive diffusion creep (e.g., Rybacki and Dresen, 2000; Tullis and Yund, 1991; Xiao et al., 2002) (Fig. 1). Estimates of lower crust viscosities as low as 10^{18}–10^{19} Pa s (Shi et al., 2015; Zhao et al., 2017) require deference of bulk rheology to weaker quartz or mica-rich phases, if present. However, if the lower crust is dominated by feldspar or stronger phases, it is difficult to reconcile such low viscosities assuming dislocation creep mechanisms, which suggests significant contributions of strain weakening and diffusion creep (Rybacki and Dresen, 2004) (Fig. 1).

In this work, we report observations from an exhumed BDT in the southern Basin and Range Province, USA. This natural exposure of a feldspar-dominated BDT provides a unique case study to compare against other quartz-dominated BDT observations. Our work includes detailed field observations, microstructural analyses, and thermochronology that allows us to define the spatial geometry of the exhumed BDT, constrain the temperature-time history, and examine its deformation conditions, which alternated between viscous and brittle during the unique heating-cooling history of this region. The study focuses on the deformed two-mica Cretaceous Ireteba granite in southern Nevada, which rotated and deformed as part of the Colorado River Extensional Corridor (CREC) in the Miocene (Kapp et al., 2002; Zuza et al., 2019). The geologic history involved ~90° rotation to exhume a crustal section across the BDT, and the well-established geologic history provides a resolved kinematic and thermal history by which to evaluate the shear zone. We discuss feldspar deformation mechanisms across this exhumed BDT and provide updated interpretations about the regional geology of CREC related to Miocene plutonism and extension.

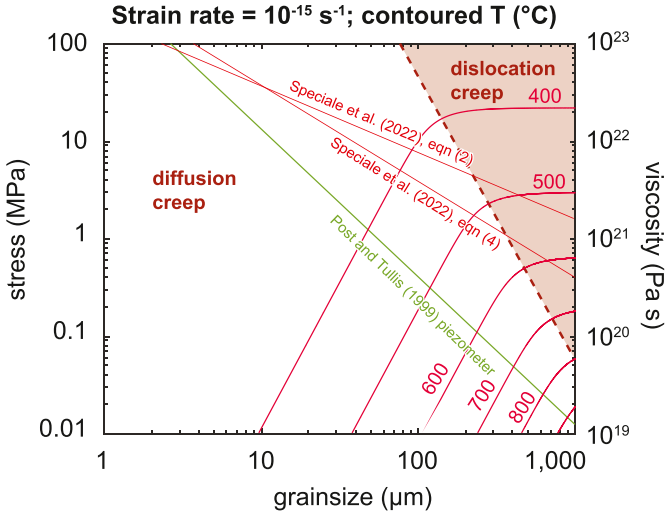

Fig. 1. Deformation mechanism map for feldspar at a constant strain rate of 10^{-15} s^{-1}. See Table 1 for relevant parameters. Note that for these strain rates, dislocation creep implies viscosities $>10^{20}$ Pa s at reasonable lower crustal temperatures.

2. Geologic setting

The study was conducted across an exhumed brittle-ductile transition (BDT) zone in the Eldorado Mountains of the CREC (Fig. 2). Here, rapid Miocene extension exhumed footwall rocks comprised of Proterozoic basement, Cretaceous granite, and pre-/syn-extensional Miocene plutons (e.g., Faulds et al., 2001, 2010; Zuza et al., 2019). The basement rocks consist of North American Proterozoic orthogneiss and migmatite intruded by the Late Cretaceous two-mica Ireteba granite (Fig. 2). The ca. 66 Ma Ireteba pluton is a biotite-muscovite-garnet peraluminous granite (Ayers et al., 2013; Kapp et al., 2002) and is part of a belt of peraluminous granites stretching from Canada in the north to Arizona in the south (e.g., Miller and Bradfish, 1980). The examined BDT crosses the Ireteba pluton.

The southern edge of the Ireteba pluton was intruded by the ca. 17.0–16.1 Ma Searchlight pluton (e.g., Bachl et al., 2001; Eddy et al., 2022; Faulds et al., 2010; Johnson, 2014). Eddy et al. (2022) presented new high-precision U–Pb chemical abrasion–isotope dilution–thermal ionization mass spectrometry (CA-ID-TIMS) zircon ages that show most of the pluton was emplaced between 17.0 and 16.2 Ma, with only the Lower Searchlight unit yielding older ages ca. 17.5 Ma. Hornblende-plagioclase thermometry and zircon-saturation temperatures suggest the Searchlight pluton was emplaced at temperatures of 750–830 °C (Bachl et al., 2001).

The Searchlight pluton intruded its own cogenetic overlying volcanic pile, at paleo-depths of ~3 km, and the pluton's base was at a paleo-depth of ~13 km, as evidenced from aluminum-in-hornblende barometry and structural restorations (e.g., Bachl et al., 2001; Faulds et al., 2010, 2002a, 2001; Zuza et al., 2019). Thus, the Searchlight pluton appears to have had a roughly ~10 by ~10 km map-view dimension and ~10 km vertical thickness at the time of its intrusion (Fig. 2). West-east crustal extension initiated almost immediately after the intrusion of the Searchlight pluton (Fig. 3) (e.g., Faulds et al., 2001). This was primarily accommodated in the study area along the east-dipping, east-directed Dupont Mountain fault (e.g., Faulds et al., 2001; Zuza et al., 2019). The footwall of this fault system tilted to the west as the hanging wall was transported to the east (Fig. 3). Zuza et al. (2019) previously interpreted that the hot footwall rocks flowed upward toward the surface during progressive removal of the hanging wall, which is reflected in distributed sub-solidus shear fabrics observed across the Searchlight pluton (Fig. 3). This model is similar to envisioned antithetic shearing related to footwall unloading described in nearby metamorphic core complexes of southern California and Arizona (e.g., Reynolds and Lister, 1990; Singleton et al., 2019; Strickland et al., 2018).

In its present-day map geometry, the top of Searchlight pluton is located to the west and the bottom is to the east (Fig. 4). The upper part of the Ireteba pluton is also located to the west, although its top is not exposed. The Dupont Mountain fault is exposed in the east, where Miocene volcanic rocks are juxtaposed over chloritized ductilely deformed, mylonitic lower Searchlight and Ireteba pluton rocks (Fig. 2). The Dupont Mountain fault currently dips moderately east (~20–40°), is well expressed as having a cataclasite zone that deforms mylonitic plutonic rocks, and displays top-east kinematic indicators (e.g., Riedel shear fractures) (Faulds et al., 2001; Hinz et al., 2012; Zuza et al., 2019). East-directed displacement on the Dupont Mountain fault decreases from ~12 km at the latitudes of the Searchlight pluton to <1 km to the north by the Aztec Wash pluton (Faulds et al., 2002b).

The timing of westward tilting of both the Searchlight and Ireteba plutons is constrained by several observations. First, the overlying Miocene volcanic rocks display westward tilt fanning (Faulds et al., 2001, 2002a, 2002b, 2010), a common feature in the Colorado River Extensional Corridor (e.g., Gans and Bohrson, 1998; Spencer et al., 2018). Specifically, ca. 16.2 Ma $^{40}Ar/^{39}Ar$ ages from the structurally higher parts of the most steeply tilted stratigraphy demonstrate the approximate initiation age of tilting and extension (Faulds et al., 2001). Volcanic strata are progressively less tilted upsection, with most of the

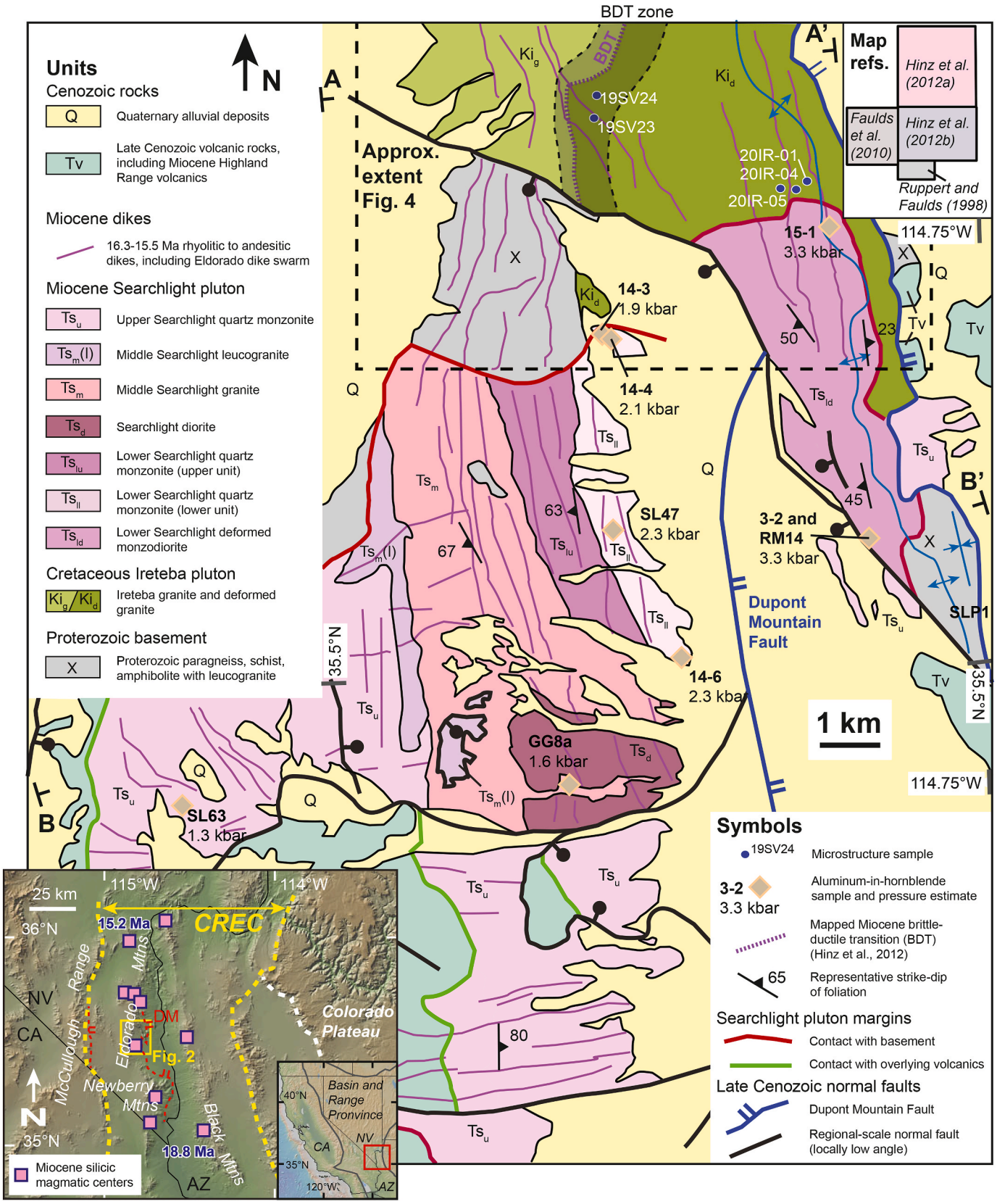

Fig. 2. Simplified geologic map of the southern margin of the Cretaceous Ireteba pluton, where it was intruded by the Miocene Searchlight pluton, southern Nevada. Inset shows 1:24,000 scale mapping sources. Map modified from Zuza et al. (2019). Cross sections A-A' and B-B' in Fig. 3. Sample locations (including those from this study and Bachl et al., 2001 aluminum-in-hornblende samples) and approximate location of Fig. 4 also shown. Paleo-BDT (BDT) shown as purple line from Hinz et al. (2012) and ~750-km-wide BDT from Rodriguez-Arriaga (2021). DM–Dupont Mountain fault. (For interpretation of the references to color in this figure legend, the reader is referred to the Web version of this article.)

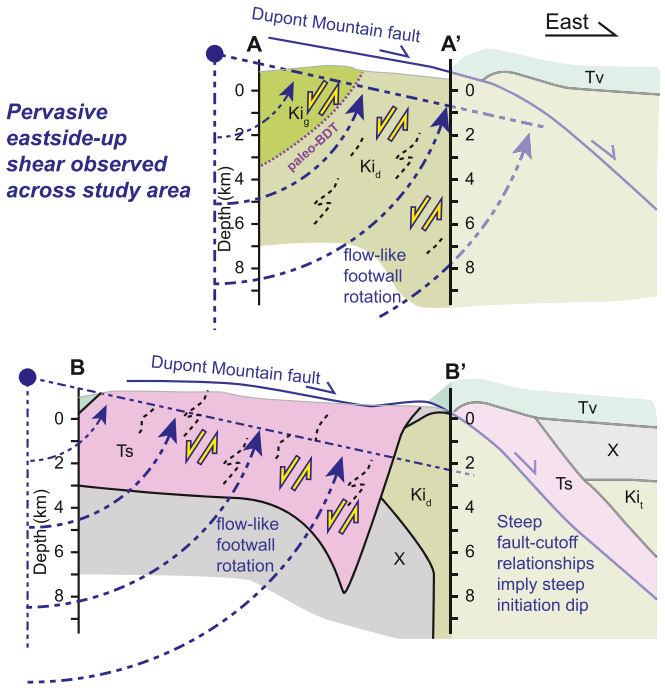

Fig. 3. Schematic cross section and tectonic model for the westward titling of the Miocene Searchlight and Cretaceous Ireteba plutons. Adapted from Zuza et al. (2019).

tilting occurring before ca. 15 Ma. Second, cross-cutting dikes, such as the ca. 15.5 Ma generally north-striking Eldorado dike swarm are east-dipping today, presumably tilted westward from a subvertical intrusion (Bachl et al., 2001; Hinz et al., 2012; Zuza et al., 2019). Both of these lines of evidence suggest rapid tilting of the system from ca. 16.2 Ma for ~0.5 Myr, tilting the crustal section here at least 60° during this timeframe. Prior (U–Th)/He thermochronology across the Searchlight pluton confirmed these timescales and rates (Zuza et al., 2019), although the zircon helium effective closure temperature (~200 °C) (Reiners et al., 2002, 2004; Wolfe and Stockli, 2010) is too low to capture the fast initial phase of rotation and exhumation.

Previous 1:24,000-scale geologic mapping across the west-tilted Ireteba pluton (Hinz et al., 2012) documented a north-trending paleo-BDT zone (Fig. 2). In this earlier mapping, Ireteba rocks west of this transitional zone were observed to be undeformed, whereas those to the east from structurally deeper levels were deformed ductilely. The age of this BDT was previously assumed to be Miocene based on its correspondence to similar structures to the south in the Miocene Searchlight pluton, although the structures and differences in deformation styles in the Searchlight pluton are less obvious due to significant heterogeneity of intra-pluton units (Hinz et al., 2012). The BDT cutting across the Ireteba pluton (1) involves similar parallel fabrics observed in the Searchlight pluton, also with top-down-west kinematics (e.g., Faulds et al., 2001), (2) distorts the Miocene Searchlight-Ireteba contact, and (3) deforms middle-Miocene dikes (Zuza et al., 2019). Furthermore, the geometric position of this paleo-BDT is compatible with the inferred westward tilting of the section and a warm geothermal gradient (e.g., 30 °C/km). The primary goal of this work was to conduct a focused traverse across this BDT zone (Fig. 4A).

3. Methods

Detailed structural and sampling traverses were conducted across the Ireteba pluton (Fig. 4). The style and kinematics of deformation along this traverse were documented, as made from field hand-sample observations, including any absence of observable deformation. Orientated samples were collected for microstructural analyses via standard stereographic observation and electron backscatter diffraction (EBSD) methods (Table 2). Thin sections were cut parallel to lineations and perpendicular to foliation.

Microstructural analyses focused on identifying the relevant phases, documenting deformation and recrystallization textures for these phases, observing shear kinematics, and measuring relict and recrystallized grain sizes. The dominant phases in most samples were plagioclase feldspar, K-feldspar, and quartz, with biotite and muscovite, minor garnet, and other accessory phases (i.e., zircon, apatite, monazite, magnetite).

EBSD analyses were conducted to get high-resolution phase maps, shear sense, determine crystallographic orientations, evaluate crystallographic preferred orientations (CPOs), relate mineral orientations to dominant slip mechanisms, differentiate subgrains, and determine grain-size (e.g., Chapman et al., 2010; Cross et al., 2017; Kruhl and Vernon, 2005; Law, 2014; Menegon et al., 2013; Miranda et al., 2016; Nevitt et al., 2017a, 2017b; Thigpen et al., 2010; Viegas et al., 2016). Polished thin sections underwent ~8 h vibrational polish with 0.02 μm colloidal silica suspension to remove near-surface crystal lattice damage. EBSD mapping was performed by collecting EBSD patterns from each node of a defined orthogonal grid using a Nordlys Nano high-resolution detector and Oxford Instruments Aztec 3.3 acquisition software package on a JEOL 7100 field emission scanning electron microscope (FE-SEM) in the Mackay Microbeam Laboratory at the University of Nevada, Reno. Map stepsize varied depending on grain size and specific goals for a given thin section, but we strove to use step sizes significantly lower than recrystallized grain-sizes to allow for grain-size evaluation (e.g., Cross et al., 2017). Postprocessing used AZtecHKL software and data was analyzed using MTEX 5.3.1 (Bachmann et al., 2010).

Several microstructural proxies were derived from the EBSD maps, including grain-size, misorientation (M) indices that describe the intensity of the fabrics (Skemer et al., 2005), and the Vollmer (1990) ternary values that describe the styles of the fabrics (i.e., R, G, P for random, girdle, and point fabrics, respectively) (Supplemental Table S1). The M index was calculated using the calcMIndex function on orientation distribution functions (ODFs) in MTEX. The R,G, and P values were determined in MTEX following methods in Mainprice et al. (2015).

Grain-size was estimated using the code of Cross et al. (2017), which differentiated recrystallized grains versus relict grains based on an internal misorientation threshold. This was adapted for feldspar grain-size estimation by removing grain twinning by merging adjacent grains with >175–180° grain misorientation. Feldspar grains in our samples appear disaggregated during deformation, and we used the geometric mean of recrystallized grains for grain-size piezometry. We considered three feldspar piezometers, including from Post and Tullis (1999) and two calibrations from Speciale et al. (2022). Evaluation of these different piezometer calibrations is beyond the scope of this study, but our recrystallized grain-size observations translate to generally similar flow stress estimates for these piezometers because the three piezometers nearly intercept in grain-size vs stress space. All quartz grains appeared recrystallized, and thus we used the root mean square (RMS) of all quartz grains with the quartz piezometer of Cross et al. (2017).

Rock fabrics formed below solidus temperatures typically show features of crystal-plastic deformation, including intra-crystal strain such as undulatory extinction and mechanical twinning as well as inter-crystal deformation including various types of dynamic recrystallization (Paterson et al., 1989, 1998). Our microstructural analyses focused on the grain distribution and boundary textures. For typical geologic strain rates, the style of quartz and feldspar recrystallization and deformation varies primarily as a function of temperature. Quartz recrystallization typically involves bulging recrystallization (BLG) at ~250–400 °C, subgrain rotation (SGR) at higher temperatures up to 400–500 °C, and grain boundary migration (GBM) at >550–500 °C (Blumenfeld et al., 1986; Blumenfeld and Bouchez, 1988; Faleiros et al., 2010; Hirth and

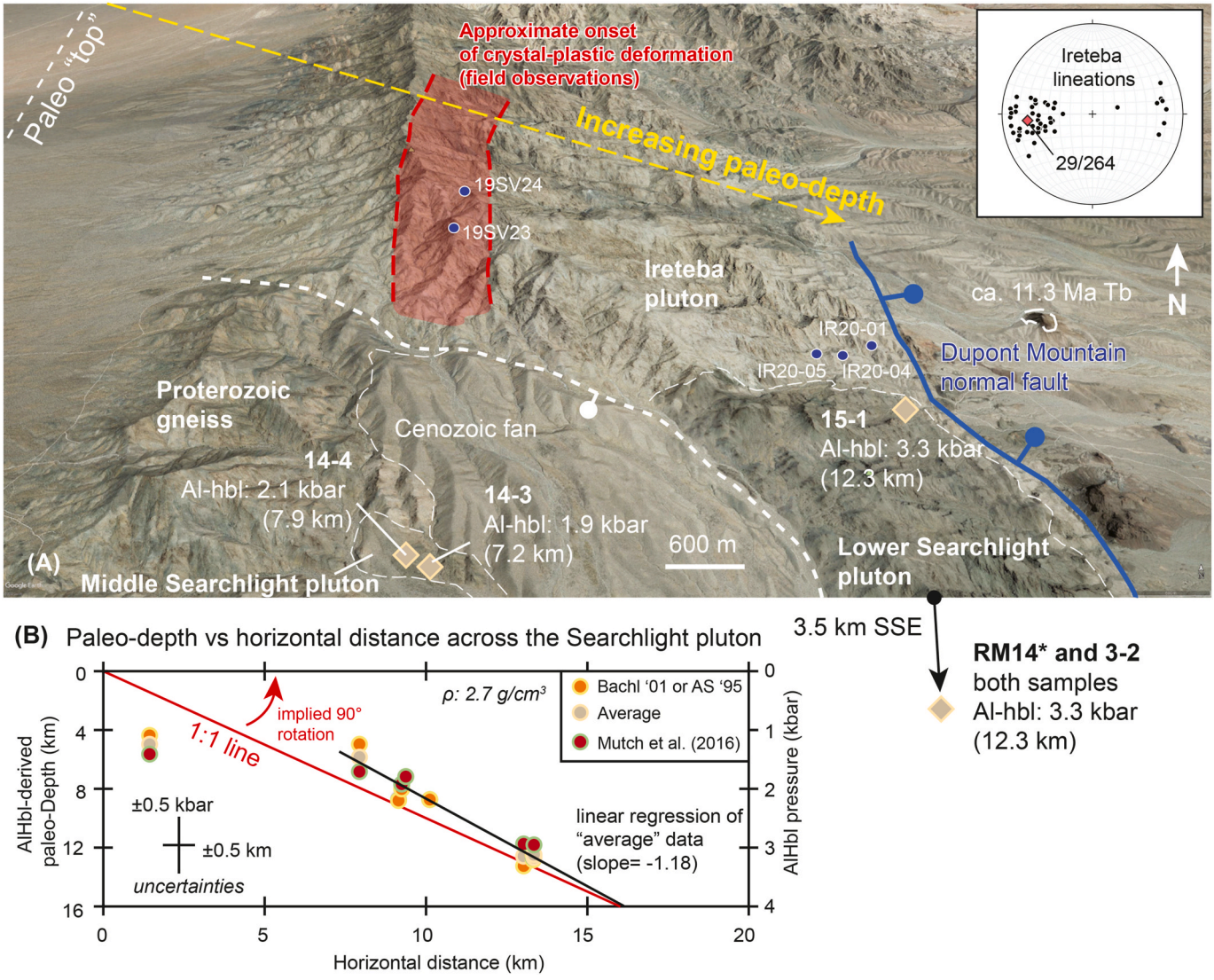

Fig. 4. (A) Oblique Google Earth view (looking north) of the main study transect across the exhumed brittle-ductile transition of the Ireteba pluton. Pluton top is in the west (left) and lower portion is in the east (right). Red zone is the approximate location of the onset of observable crystal plastic deformation in the pluton, as observed in the field, with rocks structurally higher appearing undeformed and rocks structurally lower showing evidence for sub-solidus deformation. Aluminum-in-hornblende pressure estimates (from this study and Bachl et al., 2001, denoted with *) shown with diamonds. Note samples RM14 and 3–2 were collected ~3.5 km south-southeast from this viewpoint. Inset stereonet shows west-east trending lineations from across this traverse with the first eigenvector. (B) New and compiled aluminum-in-hornblende pressure estimates vs paleo-depth as measured from the Searchlight pluton's roof. Three calibrations are shown; see text for discussion. Samples plot close to identity line, which implies that inference of 90° rotation is acceptable. (For interpretation of the references to color in this figure legend, the reader is referred to the Web version of this article.)

Tullis, 1992; Jessell, 1987; Law, 2014; Lloyd and Freeman, 1994; Mainprice et al., 1986; Stipp et al., 2002). Feldspar dynamically recrystallizes at higher temperatures than quartz, showing signs of BLG at ~450–600 °C and SGR at temperatures >500 °C (Tsurumi et al., 2003; Tullis and Yund, 1985, 1991). Below a certain crystal-plastic deformation temperature, microfaulting and fracturing can be observed. Fracturing of feldspar typically occurs below 500 °C (e.g., Passchier, 1982; Pryer, 1993). Water content, strain rate, and rock type can impact these approximate temperature-deformation conditions.

We conducted energy dispersive X-ray spectroscopy (SEM-EDS) to (1) quantify modal abundance of the phases in the coarse, relict protomylonite versus the ultramylonite and (2) semi-quantitatively explore compositional changes of the feldspar phase during deformation and grainsize reduction. Both approaches were done on the FE-SEM at UNR.

Three zircon He thermochronology traverses were conducted across the Eldorado Mountains to improve our understanding of the temperature-time history of this study region. The one across the Searchlight pluton was first reported in Zuza et al. (2019) and here we have added more data. The northern traverse was across the Miocene Aztec Wash pluton and the southern was across the Miocene Spirit Mountain batholith, and are new to this study. Detailed analytical methods are reported in the Supplemental Materials.

To confirm paleo-depth constraints, we conducted aluminum-in-hornblende (AlHbl) barometry that supplements that of Bachl et al. (2001) from the Searchlight pluton, <1 km south of the study traverse (Figs. 2 and 4). The apparent 1:1 linear correlation between eastward distance from the paleo-Searchlight-pluton roof and igneous crystallization depth inferred from the AlHbl Bachl et al. (2001) barometry suggests the entire system was rotated ~90°. We conducted 5 additional AlHbl barometry analyses, using both the Anderson and Smith (1995) and Mutch et al. (2016) calibrations. Bachl et al. (2001)'s dataset is based on the Anderson and Smith (1995) calibration, but we recalculated pressures using Mutch et al. (2016). Our analyses are comparable to those of Bachl et al. (2001), and our final reported AlHbl pressure

Table 1
Parameters used to construct deformation mechanism map.

	Dislocation creep	Diffusion creep	Piezometers 1	2	3	Explanation
Aggregate	An_{60}	An_{60}				Labradorite
log A (MPa^{-n} μm^m s^{-1})	−1.5	1.1				Material constant
Q (kJ mol^{-1})	235	153				Activation energy
n	3	1				Stress exponent
m	0	3				Grain-size exponent
H_2O (wt%)	0.3	0.3				Water
Ap			55	$10^{3.30}$	$10^{2.59}$	Piezometer material constant
Mp			−0.66	−1.47	−1.01	Piezometer exponent
Reference	1	1	2	3	4	
Fixed parameters, depending on map						
Strain rate (s^{-1})	10^{-11} s^{-1}	10^{-11} s^{-1}				Axial strain rate
Temperature (°C)	600	600				

References.
1. Dimanov et al. (unpublished) cited by Rybacki and Dresen (2004).
2. Post and Tullis (1999).
3. Equation (2) of Speciale et al. (2022).
4. Equation (4) of Speciale et al. (2022).

Table 2
Analyzed EBSD samples.

Sample	Latitude	Longitude	Elevation (m)
19SNV24[a]	35.58878	−114.822	1451
19SNV23	35.58356	−114.822	1390

[a] 19SNV24 includes sub-samples a,b,c, and d.

values are averages of either (1) Bachl et al. (2001)'s data with the Anderson and Smith (1995) calibration and our re-calculation of the data using the Mutch et al. (2016) relationship, or (2) our new data averaged between the Anderson and Smith (1995) and Mutch et al. (2016) calibrations. We assume pressure uncertainties of ±0.5 kbar, which is more conservative than reported by either calibration. Full methods are in the Supplemental Material and Supplemental Tables (Tables S6 and S7).

4. Results and observations

4.1. Field observations

The western extent of the studied traverses representing the brittle and the uppermost portion of the crust, consists of Ireteba granite that preserves magmatic textures, with discrete brittle faults and fractures, but lacks penetrative ductile deformation (Fig. 5A). The pluton consists of coarse grained subhedral to euhedral K-feldspar (5–25 mm; 45–55%), plagioclase (5–15 mm; 25–35%), and quartz (5–15 mm; 25-15%) with fine to medium grained (1–3 mm) subhedral biotite and muscovite (~5%). Mineral alignment is not common in this portion of the pluton. In hand sample, minerals are not aligned, and there is no discernible sub-solidus or magmatic fabric (Fig. 5A).

The mapped BDT is a 750 m-wide zone structurally beneath the "brittle" part of the section (Rodriguez-Arriaga, 2021). In the field we approximately define an upper and lower BDT boundary. The upper BDT boundary exhibits the onset of sporadic discrete, fine-grained ductile shear zones. The bottom boundary of the BDT is less well constrained because the ductile deformation becomes more and more distributed. We place the bottom of the BDT at the approximate location where penetrative shear fabrics and lineations dominate the outcrops, with all quartz and feldspar appearing dynamic recrystallized.

The upper BDT boundary is approximately located at ~2 kbar based on new and existing AlHbl pressure estimates, which is ~7.6 km depth (samples 14–4 and 14–3 in Fig. 4). There is a northwest-striking, southwest-dipping normal fault between the closest AlHbl datapoint on this BDT, which may obfuscate the relationship between BDT and these AlHbl pressure estimates. An alternative constraint comes from sample 15-1—with a pressure estimate of ~3.3 kbar (12.3 km) (Fig. 4)—which is located ~4 km east, or paleo-down section, from the top of the BDT zone across continuous non-faulted Ireteba and Searchlight pluton. This datapoint suggests the BDT zone is depth is ~8.3 km, broadly similar to the first estimate.

Moving east, or paleo-down section (Fig. 4A), within the BDT, quartz show more signs of sub-solidus deformation, appearing as ribbons or flattened grains. More pronounced deformation features start to be observed, including very localized shear bands, either expressed as 1 cm to 10 cm-scale zones with sub-solidus feldspar and quartz grains forming CS-fabrics, or ~1-cm-scale discrete mylonitic shear zones (Fig. 5C and D). Both types of deformation show similar top-down-west shear kinematics. Lineations here trend west. Less deformed coarse grains get warped into the discrete mylonite zones and clearly show the shear sense in outcrop. Going east across this zone, the density and size of local shear structures increases. In one location, a ~20-cm thick ultramylonite zone comprised predominately of feldspar is observed (Fig. 5B).

These localized shear zones are not evenly or continuously distributed across the BDT. They are separated by less ductily deformed blocks of granite wallrock, suggesting the strain is partitioned into different parts of the granite. At one location within the BDT, across a 5 m transect, there is a clear gradient from nearly undeformed granite to ultramylonite (Fig. 6A–C). During this transition, quartz is strung out as ribbons, and grain-size reduction is dramatic, from cm-to micron-scale. Shear fabrics show similar top-down-west shear. Roughly ~750 m east (i.e., structurally lower), fabrics and lineations become very distributed, and most outcrops appear homogenously sheared and deformed. At this approximate position, we define the base of the BDT, which thus has a ~750 m width in map view and similar paleo-vertical thickness.

Further to the east, at the bottom of our structural traverse, deformation is observed to be very distributed (Fig. 5E). Fabrics dip more gently west and east, and the lowest exposures are involved in a north-trending antiform related to the Dupont Mountain fault (Fig. 2; Hinz et al., 2012). Across the fold hingeline, foliation change dips from moderately west (~20–50°W) to moderately east (~10–40°E) (Fig. 2). Here lineations within the Ireteba pluton are more strongly developed than foliations (i.e., $L > S$; L or LS tectonites), which are commonly absent. Quartz is mostly observed as ribbons defining stretching lineations that trend west or east. At these structurally lower exposures, discrete mylonite zones with severe grain-size reduction are not observed. Most outcrops display either top-west shear kinematics or ambiguous shear-sense indicators. Mylonitic fabrics associated with the

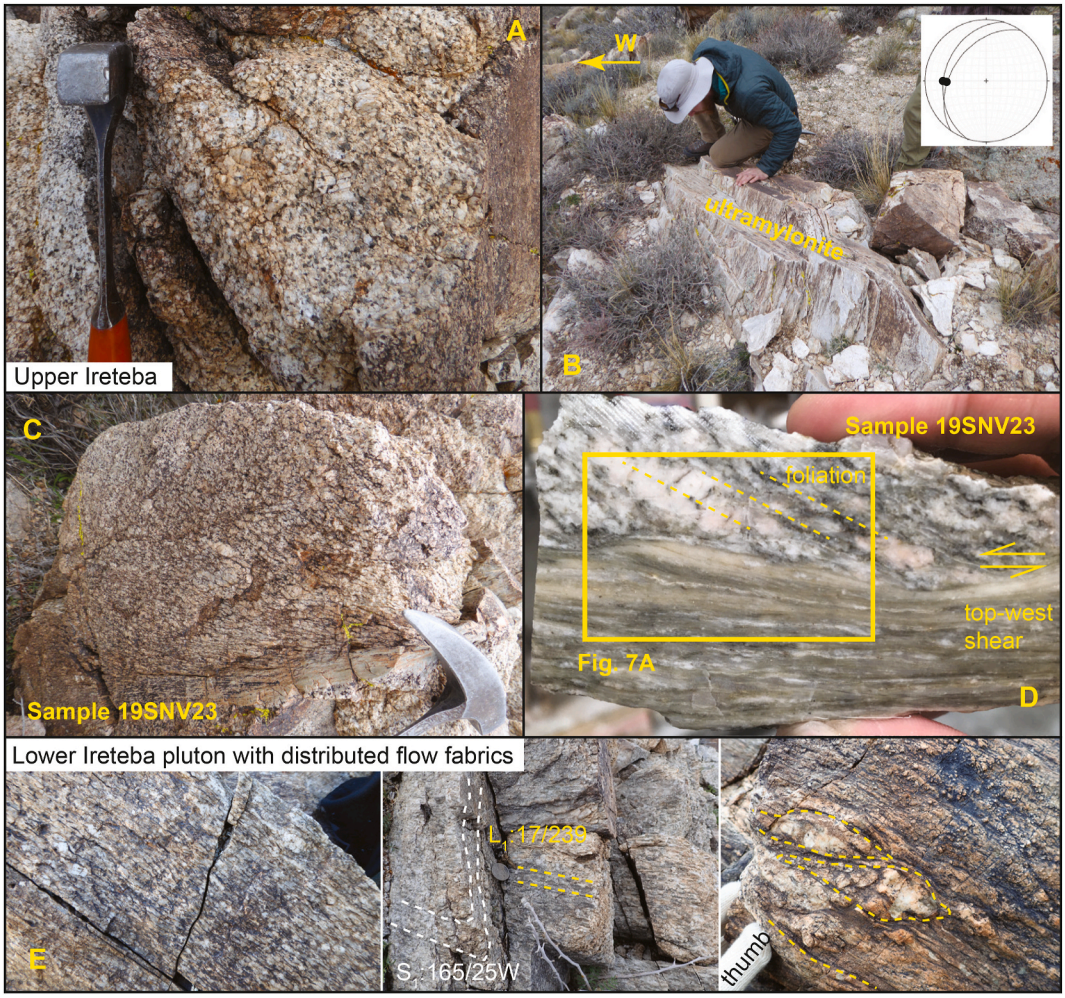

Fig. 5. Field photographs from across studied traverse, showing range of deformation textures and characteristics. (A) Undeformed upper Ireteba pluton. (B) Ultramylonite exposure with attitude data (foliation lineations plotted on inset stereonet) near sample 19SNV24 (see Fig. 6). (C) Exposure of sample 19SNV23 (see Fig. 4A) and (B) slab cut across the transition from the coarse granite to ultramylonite (yellow box shows thin section in Fig. 7A). (E) Lower Ireteba pluton showing distributed ductile flow fabrics. (For interpretation of the references to color in this figure legend, the reader is referred to the Web version of this article.)

Dupont Mountain fault are observed within ~100 m of the fault (e.g., Zuza et al., 2019).

4.2. Microstructure observations

Microstructural analysis was focused on the brittle-ductile transitional zone at sample localities 19SNV24 and 19SNV23 (Fig. 4). Sample 19SNV23 was collected from an outcrop that shows coarse protomylonitic foliations warped into a discrete ultramylonitic shear zone (Fig. 5C and D). A thin-section scan across this transition is in Fig. 7A. The sample consists of K-feldspar, plagioclase, and quartz, in order of relative abundance. The shear-zone geometry shows top-west shear. Brittle fractures across the thin section are consistent with R and R′ shear fractures in orientations consistent with top-west shear (Fig. 7A). The R and R' shear fractures do not cut into the ultramylonite at the bottom of the sample (Fig. 7A). Coarse (>1 cm) feldspar phases defined foliations that transition into the <20 μm grain-size ultramylonite at the bottom of the thin section.

An EDS map for sample 19SNV23 was overlain on the thin-section scan in Fig. 7A. Normalized EDS maps (i.e., pixeled without significant Ca or K removed) reveal 63:37 K-feldspar:plagioclase ratios in the protolith and 67:33 ratios in the ultramylonite, suggesting no significant change in mineral abundance. All analyzed fields reveal a K-feldspar-to-plagioclase ratio of 65:35.

EBSD maps were made across the coarse protomylonite and the ultramylonite. The large coarse K-feldspar grain (Fig. 7C) displays an inherited CPO, with M indices >0.4 and R values of 10–30% (Fig. 7D) (Supplemental Table S1). C axes concentrate in the center of a lower hemisphere pole figure (i.e., the *Y* axis). This grain shows subgrain development (~20 μm) that increase in density and misorientation to the left, approaching the discrete high-angle shear zone (Fig. 7E–G). EBSD inverse pole figure (IPF) maps show two linear shear zones (R-R′ fractures) with discrete offsets are observed cutting the larger feldspar grains (Fig. 7C). The shear zones are at a high angle (80°) and low-angle (30°) to the main mylonite in the lower part of the shear zone. The low-angle shear zone (R fracture) displaces a K-feldspar twin down to the left (Fig. 7C), with kinematics consistent to the main mylonitic shear zone. The steep R′ fracture is presently comprised of interlocking K-feldspar grains with a strong inclined shape-preferred orientation (SPO) that suggests right-side down kinematics (Fig. 7C). Both kinematics are consistent with overall top-down-west shear in the sample, as observed in outcrop (Fig. 7C). Recrystallized grains within the R-R′ fractures display fine grain-size (~18 μm average), an annealed interlocking grain texture, and moderate CPO (M: 0.16) (Fig. 7H). Fig. 7H shows the subgrain development in the larger K-feldspar grain and strong SPO within the R-R' fractures.

In the ultramylonite part of sample 19SNV23, plagioclase and K-feldspar define aggregate bands that are distributed across the shear

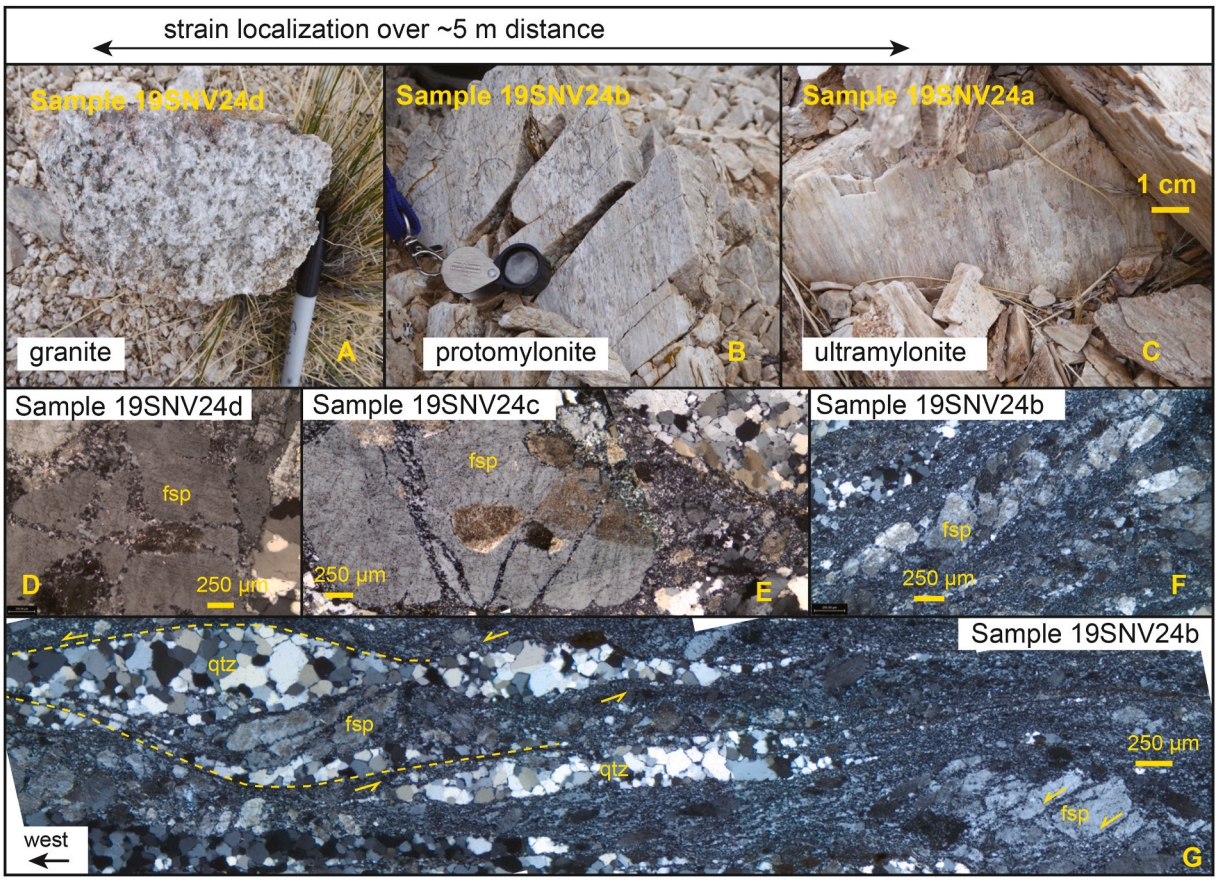

Fig. 6. Field and microstructural observations across the traverse of sample 19SNV24. (A–B) Transition across ~5 m from undeformed granite to ultramylonite at sample location 19SNV24 (see Fig. 4A for location). Photomicrographs showing (D) brittle fractures across feldspar (fsp) grains in the relatively undeformed sample 19 SNV24d, (E) brittle fracturing and cataclasis of feldspar in more strongly strained sample 19SNV24c, and (F) fracture and disaggregation of feldspar in sample 19SNV24b. These images demonstrate the importance of grain-size reduction via brittle fracture and cataclasis. (G) A mosaic of photomicrographs from sample 19SNV24b showing brittle fractures and antithetic rotation of feldspar (bottom left) and sigmoidal quartz (qtz) ribbons demonstrating top-west shear (top-down-west shear sense).

zone, and grain-size is reduced 5.5 ± 3 µm and 7.4 ± 5 µm, respectively (Fig. 7I) (Supplemental Table S1). This suggests flow stresses near ~50 MPa (Post and Tullis, 1999; Speciale et al., 2022). There is no discernible CPO for the feldspar grains (Fig. 7I): M equals ~0.01 and R is 90–95% (Fig. 7I) (Supplemental Table S1). As mentioned above with the EDS mapping, the proportion of quartz and feldspars is similar to the protomylonite part of the sample. Quartz is distributed in ribbons with a recrystallized grain size of 41 ± 20 µm and a moderate-weak CPO (M: 0.05) (Fig. 7I). This recrystallized grain size equates to ~40 MPa stresses (Cross et al., 2017). C axes plot near the Y axis of the pole figure, suggestive of prism <a> slip.

At sample location 19SNV24, undeformed granite (sample 19SNV24a) gradually transitions into an ultramylonite (sample 19SNV24d) across a 5 m wide exposure (Fig. 6). In thin section, this transition involves generation of distinct quartz bands and grain-size reduction of feldspar. Observations of increasing feldspar fracturing and cataclasis (Fig. 6D–G) provides information on the mechanisms of grain-size reduction. In sample 19SNV24b (Fig. 6B), feldspar grains are heavily fractured and show signs of disaggregation (Fig. 6F and G). This sample also shows antithetic feldspar fracturing and sigmoidal quartz ribbons consistent with top-down-west shear (Fig. 6G).

The ultramylonite (sample 19SNV24d) (Fig. 8A) has quartz ribbons with an average grain size of ~48 ± 22 µm (Supplemental Table S1), which equates to ~40 MPa flow stress (Cross et al., 2017). Quartz c axes reveal a weak CPO (M: 0.04) defining a girdle with a weak maxima near the Y axis of the pole figure (Fig. 8C). Asymmetry to the weak girdle suggests top-west shear for this sample (Fig. 8C). This c-axis distribution hints at combined prism, basal, and rhomb <a> slip systems. Low-angle (5–10°) misorientation axes show rotation about the c axis, consistent with significant prism <a> slip (Neumann, 2000) (Fig. 8C).

Plagioclase and K-feldspar EBSD phase maps demonstrate that the phases are well mixed. Grains have planar straight grain boundaries, and four-way grain boundaries are observed. Feldspar grain-size is ~6–8 µm and ~7–11 µm for plagioclase and K-feldspar, respectively, depending on the analyzed location within the sample (Supplemental Table S1). These recrystallized grain sizes are consistent with stresses of ~50 MPa (Post and Tullis, 1999; Speciale et al., 2022). There is weak-to-no discernible CPO, and M and R indices are 0.01–0.03 and 75–95%, respectively (Fig. 8B,E) (Supplemental Table S1).

In the lower Ireteba pluton, outcrops are strongly lineated (Fig. 10A) with a variably well-developed to weakly expressed foliation (Fig. 10B). Observed thin sections for two samples (IR20-01 and IR20-04, location in Fig. 3A) display moderate grainsize reduction of quartz and feldspar, with polyphase quartz-feldspar aggregates having grainsizes mostly >100 µm (Fig. 10C and D). In thin section, both quartz and feldspar show a shape-preferred orientation with long axes parallel to lineations and short axes orthogonal. Quartz grain boundaries are interlobate and amoeboid, suggestive of grain-boundary migration recrystallization, and undulose extinction is observed within the quartz grains (Fig. 10C and D). Feldspar exhibits deformation twinning, and bulging and subgrain-rotation recrystallization textures along its grain boundaries (Fig. 10C and D). We conducted EBSD analyses on sample IR20-05 (location in Fig. 3A) focused on its relatively pure quartz ribbons. Coarse grains (diameter greater than hundreds of µm) exhibited a weak

Sample 19SNV23

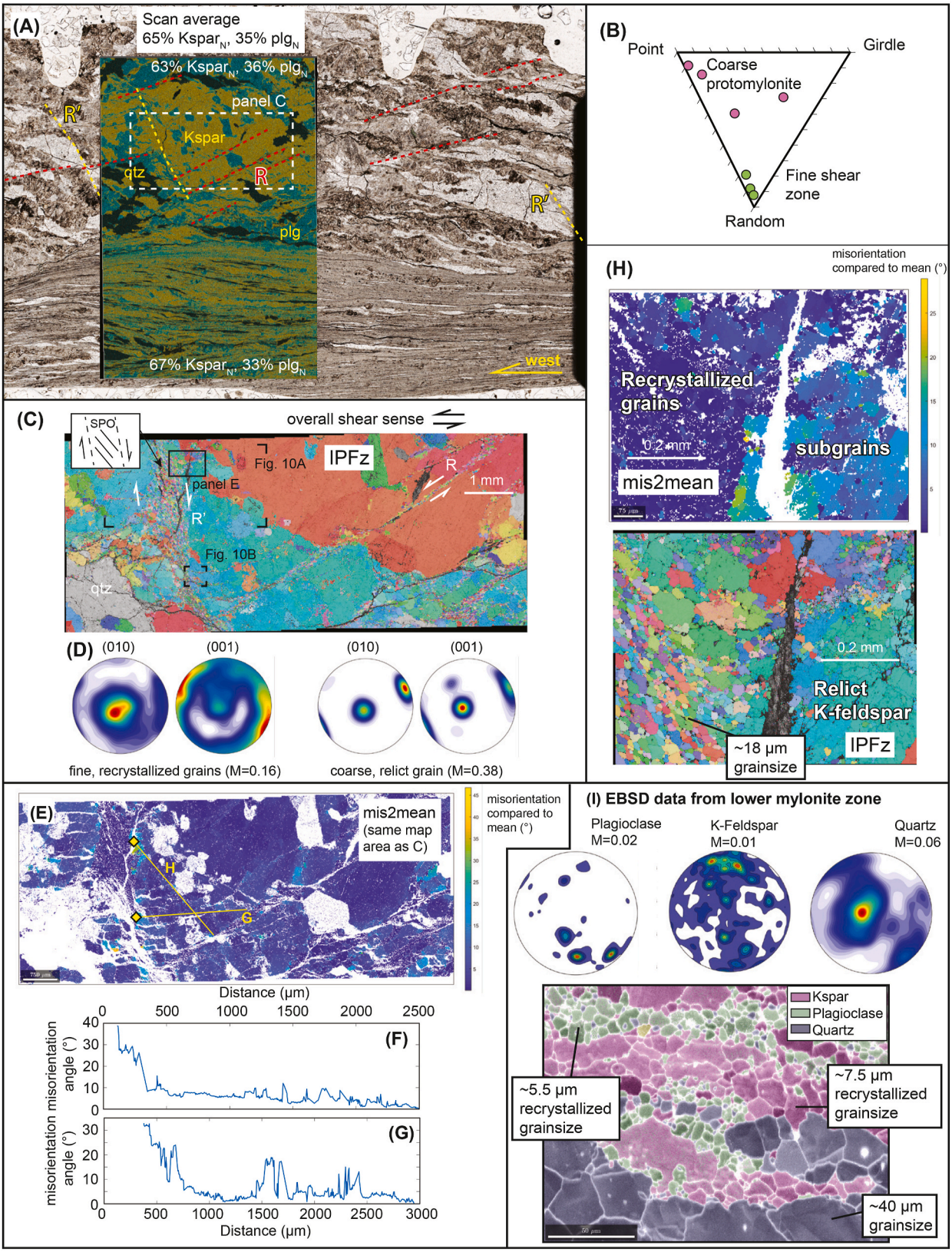

(caption on next page)

Fig. 7. Microstructural observations from sample 19SNV23. (A) Thin section scan of the sample, overlain with an energy dispersive X-ray spectroscopy (EDS) map to calculate modal percent of K-feldspar (Kspar) vs plagioclase (plg). Red and yellow dashed lines show discrete shear factures interpreted as R and R′ shear planes, respectively. (B) Summary point (P)-girdle (G)-random (R) ternary (Vollmer, 1990) showing EBSD crystallographic preferred orientation (CPO) constraints for the coarse vs fine regions of this sample. (C) IPF-Z map of a large K-feldspar porphyroclast cut by the interpreted R and R′ shear planes. Location of panel E is shown across the R′ shear with a shape-preferred orientation (SPO). (D) Pole figures of (010) and (001) axes showing moderate CPO for the finely recrystallized grains in the shear zone shear zones and a inherited CPO for the large relict grain. (E) Mis2mean map of same area as C showing misorientation traverses in G and H. (F–G) Misorientation profiles (locations in E) showing increasing subgrain development toward the left grain boundary. (H) Misorientation compared to mean (mis2mean) and IPF-Z map of R′ shear zone. Note subgrain development toward the margins of the relict K-feldspar phase and the strong SPO of recrystallized grains. (I) Pole figure plots of c axes for plagioclase and K-feldspar from the ultramlyonite at the bottom of the thin section, showing no CPO. (For interpretation of the references to color in this figure legend, the reader is referred to the Web version of this article.)

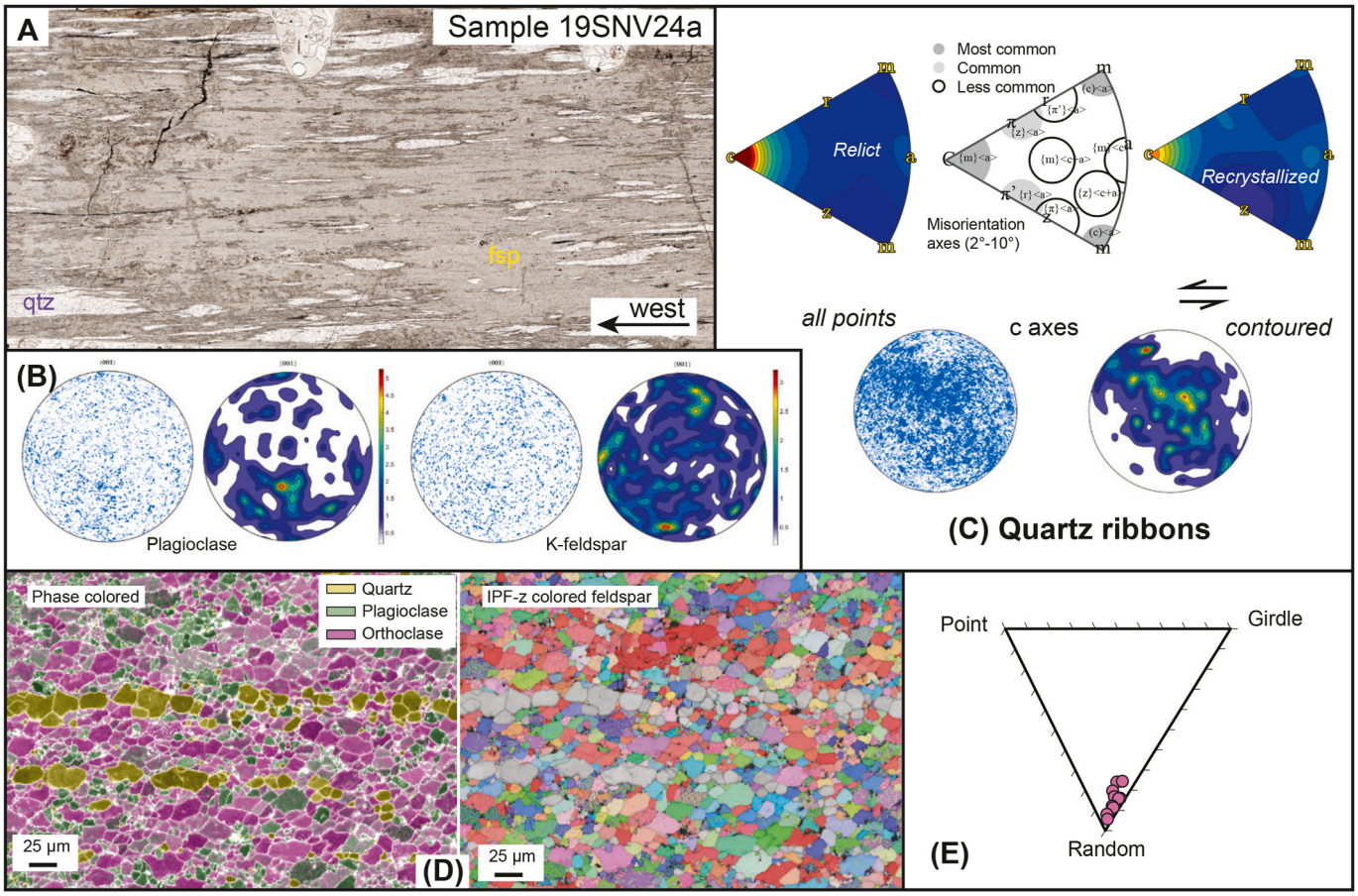

Fig. 8. (A) Thin-section scan of the sample showing ultramylonite texture of mostly feldspar with light color quartz ribbons. (B) Pole figure plots of c axes for plagioclase and K-felspar, showing no CPO. (C) EBSD data from quartz ribbons, including low-angle (5–10°) misorientation axes on an inverse pole figure for the relict and recrystallized grains, a legend to interpret the misorientation plots (Neumann, 2000), and c axes. (D) Phase map and IPF-Z map (only feldspars). Note four-way straight grain boundaries and lack of CPO suggest grain-boundary sliding deformation mechanisms. (E) Point-girdle-random ternary (Vollmer, 1990) showing EBSD crystallographic preferred orientation (CPO) constraints for this sample from different maps. fsp–feldspar; qtz–quartz. (For interpretation of the references to color in this figure legend, the reader is referred to the Web version of this article.)

CPO in both quartz and feldspar (Supplemental Table S1). Given the weak CPO and relatively coarse grainsize, we do not further interpret or discuss the deformation in the lower Ireteba pluton in this present study.

4.3. Feldspar compositional changes via EDS analyses

Semi-quantitative normalized EDS analyses focused on sample 19SNV23 to explore how feldspar composition changed during progressive deformation and grainsize reduction. The focus areas overlap the EDS compositional map (Fig. 7). Compositional changes were explored by comparing CaO weight % variations, which is parallels the anorthite content of the analyzed feldspars. All analyzed K-feldspar were ~90% orthoclase.

The relict plagioclase grains span CaO values of 2–4 wt % (average ~3.4 wt%) (Fig. 10). The ultramylonite part of the sample (lower part of Fig. 7A) has similar plagioclase CaO contents of 2–4 wt % (average ~2.9 wt%) (Fig. 10). The recrystallized R' shear zone (e.g., Fig. 7C) displays anomalously lower values of <1.5 CaO wt % (Fig. 10). Of note, there are several late-stage cracks that cut across grain boundaries, and some of these have thin rims of recrystallized plagioclase feldspar around them (Fig. 10A and B). Plagioclase around these cracks have a mixed range of plagioclase CaO contents of 0.5–3 to wt % (Fig. 10D). Chlorite is observed along some of these late-stage cracks (Fig. 10A), but is generally rare in the sample.

4.4. Low-temperature thermochronology

Twenty samples were analyzed for ZHe analyses from the Miocene

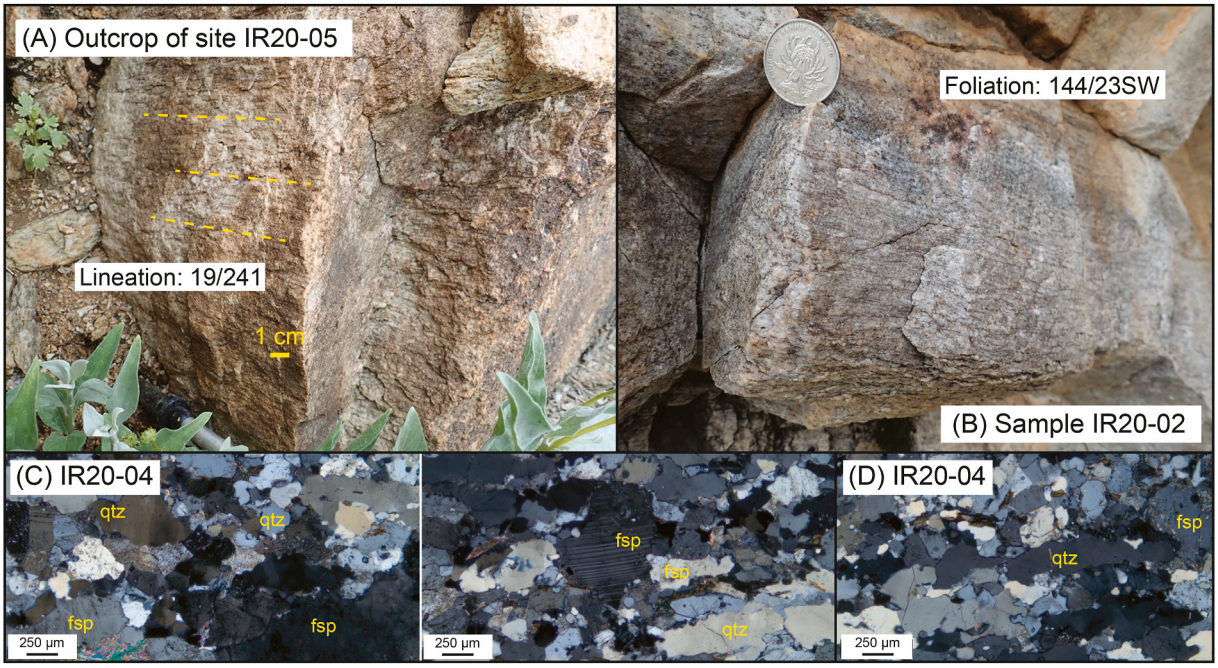

Fig. 9. Characteristics and microstructural observations from the lower Ireteba pluton. Sample locations in Fig. 4 (A) Outcrop photograph of the strongly lineated Ireteba pluton. Planar foliation is cleavage and an aligned-mineral foliation was very weakly developed. (B) Outcrop of strongly lineated and foliated Ireteba pluton. (C,D) Photomicrographs of Irteba pluton samples showing dynamic recrystallization textures of quartz (qtz) and feldspar (fsp).

Aztec Wash pluton (ca. 15.7 Ma crystallization age) (Falkner et al., 1995), Searchlight pluton (ca. 16.2–17.0 Ma crystallization age) (Bachl et al., 2001; Eddy et al., 2022; Faulds et al., 2010; Miller et al., 2006), and Spirit Mountain Batholith (ca. 16.1–17.7 Ma crystallization age) (Claiborne et al., 2006; Walker et al., 2007) (Fig. 11A). Complete data tables are in Supplemental Tables S2, S3, S4, and S5. Most analyses yielded Miocene dates, and individual aliquots that resulted in dates older than the intrusive ages were excluded ("X" symbols in Fig. 11). For each sample, a mean age was calculated, and we plotted the data against a restored structural position considering the published magnitudes of block rotation with ~1 km vertical uncertainty. This distance was measured downward from a datum at the observed top of the Miocene volcanic rocks based on published geologic maps (see Supplemental Table S5 for description) (Claiborne et al., 2010; Falkner et al., 1995; Faulds et al., 2001, 2002a; Harper et al., 2004; Hinz et al., 2012; Walker et al., 2007). In general, within uncertainty, all three traverses show ca. 12 to 15 Ma cooling, with younger ages in structurally deeper positions (Fig. 11). Samples below the approximate PRZ zone (calculated assuming 30 °C/km thermal gradient and 200 °C closure temperature) yield similar ages to those above (Fig. 11).

For the Aztec Wash traverse analyses below the PRZ appear to show a younger trend with greater depth. This trend starts at ~7 km depth, which may thus represent an approximate location of the PRZ (Fig. 11B). This constrains the geothermal gradient to ~29 °C/km, which is similar to what we inferred. The ZHe data also shows a noteworthy number of individual aliquots from all traverses that yielded ca. 10–11 Ma ages that were significantly younger than the rest of the analyses (Fig. 11).

4.5. Aluminum-in-hornblende barometry results

AlHbl barometry results for the Searchlight pluton are presented in Supplemental Table S6. The 5 newly analyzed samples yielded pressures from 1.9 kbar to 3.3 kbar, or ~7 km–~12.5 km (i.e., assuming the overburden rock has a density of 2.7 g/cm^3). Bachl et al. (2001)'s barometry results for 4 samples are in Supplemental Table S7, including our recalculations using the Mutch et al. (2016) barometry calibration. We measured the map-view horizontal distance east from the assumed paleo-roof of the Searchlight for all samples (Supplemental Table S8), and plotted interpreted paleo-depth versus map-view distance in Fig. 4B. Samples broadly plot along a 1:1 line, as previously observed by Bachl et al. (2001), which supports that this system rotated ~90° westward. The furthest west sample, from the upper part of the Searchlight pluton, plots below the 1:1 line, perhaps suggesting less rotation of the upper part of the pluton during footwall rotation. A linear regression of all data yields a slope of −0.7, which cannot be interpreted in the context of rigid-body rotation because that implies that the samples are further apart horizontally today than their initial vertical separation. Alternatively, a linear regression of all but the shallowest sample yielded a slope of −1.18 (Fig. 4B), which implies ~80° westward rotation. For the purpose of this study, we argue that this dataset confirms that an assumption of ~90° westward rotation is valid.

5. Discussion

5.1. Deformation styles at brittle-ductile transition depths

Deformation varied significantly across the Ireteba pluton. The lower Ireteba pluton showed distributed flow-like conditions, whereas the paleo-position of the Miocene BDT (Fig. 4) displayed discrete ultramylonite ductile shear zones in less strained host rock. At the structurally highest positions, the pluton was undeformed or brittlely fractured. The structurally lower levels were coarse grained. Observations of grain boundary migration recrystallization in quartz and subgrain rotation recrystallization of feldspars suggests relatively hot deformation conditions >500–600 °C (Bestmann and Prior, 2003; Blumenfeld et al., 1986; Mainprice et al., 1986; Stipp et al., 2002). Conversely, within paleo-BDT, quartz EBSD observations are consistent with prism <a> or combined basal, prism, and rhomb <a> slip. This range of slip systems may have been operative at temperatures of 400–600 °C (e.g., Lloyd and Freeman, 1994; Stipp et al., 2002). Although these are broad semi-qualitative temperature ranges, the differences in quartz slip activity and dynamic recrystallization are consistent with the structurally lower rocks deforming at higher temperatures than those structurally higher samples from within the BDT (Fig. 4).

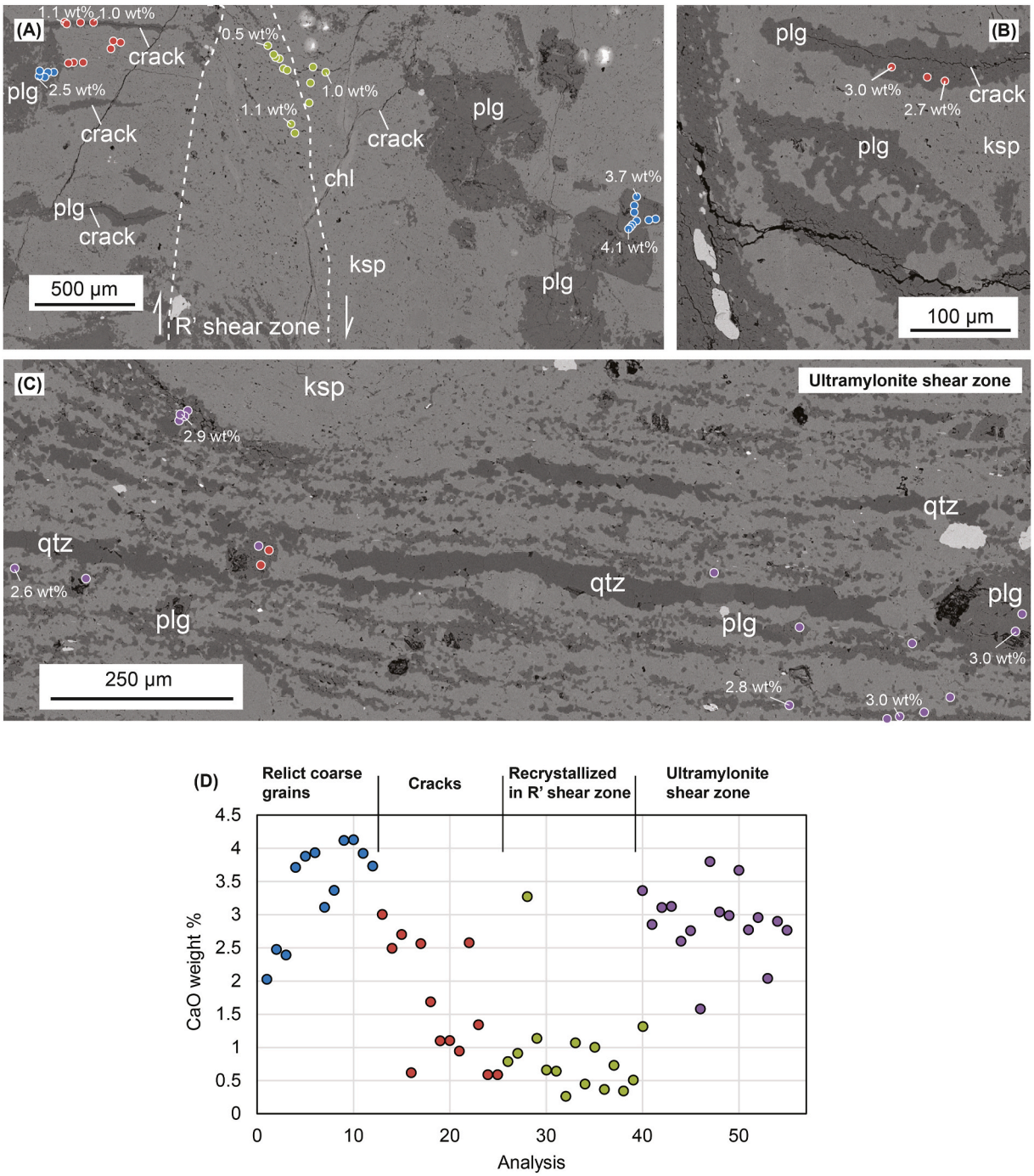

Fig. 10. Compositional variations of plagioclase in sample 19SNV23. (A–C) Scanning electron microscope backscatter images (west is to the left, as in Fig. 7A) of (A) the R′ shear zone and (B) recrystallized crack, and (C) the ultramylonite zone in the lower part Fig. 7A. Spots indicate analyzed energy dispersive X-ray spectroscopy (EDS) locations, color-coded by location, as explained in panel D. (D) Plot of CaO weight % versus analysis number, differentiated by analyses of the relict coarse grains (blue), spots near cracks (red), grains in the finely recrystallized R′ shear zone (green), and spots from the ultramylonite zone (purple). Spot locations in panels A–C. Complete data in Supplemental Table S9. plg–plagioclase; ksp–K-feldspar; qtz–quartz.; chl–chlorite. (For interpretation of the references to color in this figure legend, the reader is referred to the Web version of this article.)

Observations from our structural traverse support previous interpretations that the Ireteba pluton exposes a Miocene brittle-ductile transition (Hinz et al., 2012). We interpret a Miocene age for this BDT because the position and kinematics correlate with similar shear zones observed across the Searchlight pluton to the south (Zuza et al., 2019). Map relationships, structural considerations, and AlHbl pressures suggest that this BDT would have been located at a paleo-depth of ~7–8 km prior to Miocene tilting. At warm thermal gradients (30–40 °C/km) this paleo-depth implies temperatures of ~300 °C. However, based on the proximity to the intruded Miocene pluton, it is likely that this paleo-BDT structural level was hotter at 500–600 °C and subsequently cooled to <300 °C during exhumation and conductive cooling.

At the approximate paleo-position of the Miocene BDT (Fig. 4), a range of seemingly coeval, overprinting deformation conditions were observed. Brittle R and R' shears were observed in samples 19SNV23 and 19SNV24a with top-down-west shear kinematics (Figs. 5–8). These structures are overprinted by (1) dynamic recrystallization of feldspar within the shear planes (Fig. 7C) and (2) the ultramylonite that transects

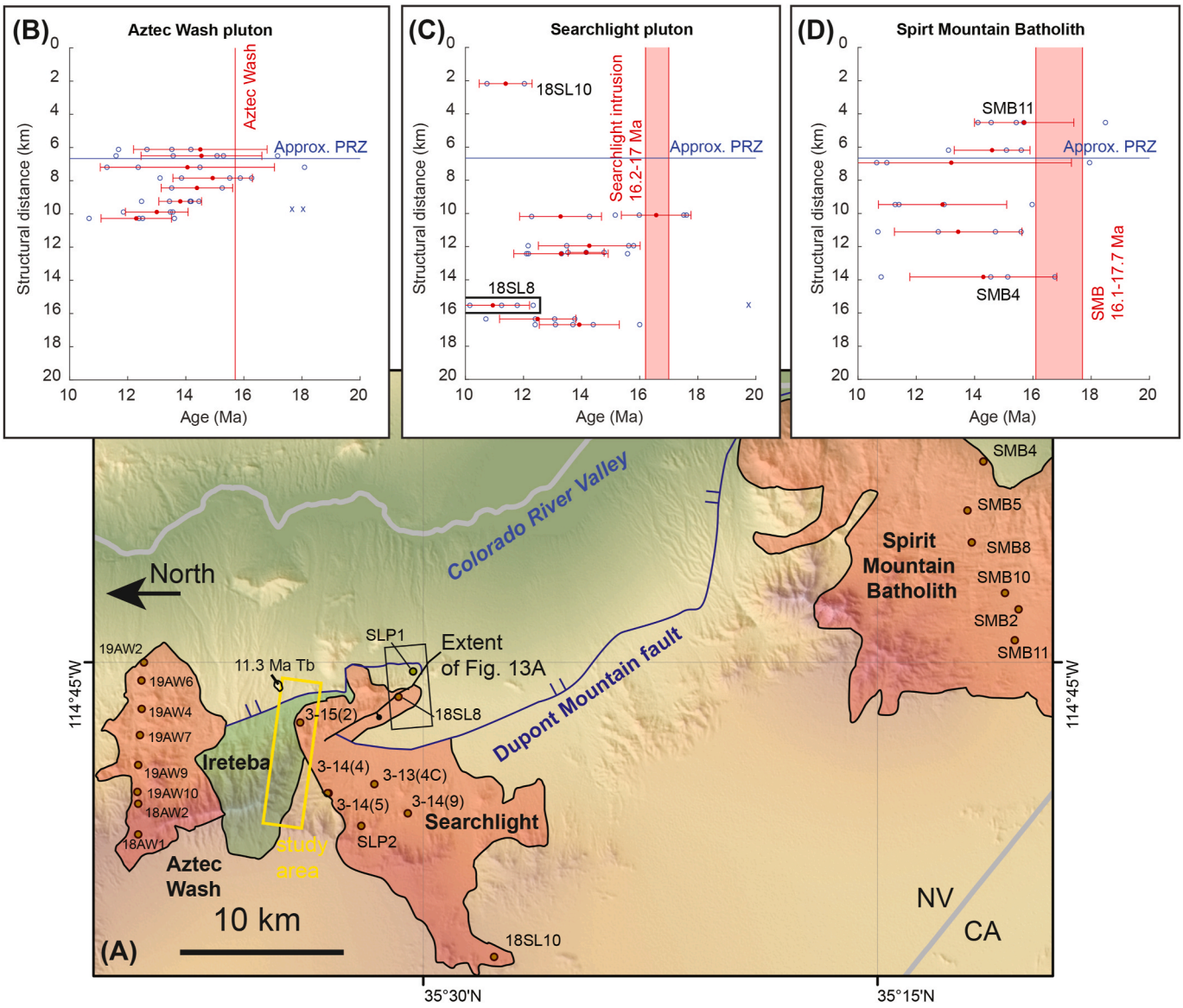

Fig. 11. Zircon (U–Th)/He thermochronology (ZHe) results from this study and Zuza et al. (2019). (A) Map shows the three traverses Miocene plutons and sample locations. (B–D) ZHe results as single aliquot dates (blue circles), sample mean and standard deviation (red symbols), analyses excluded from the mean (X), approximate Miocene intrusions ages (red lines/shading), and approximate ZHe partial retention zone (PRZ) depth assuming a 200 °C ZHe closure temperature and 30 °C/km thermal gradient. Structural position based on inferred tilt of the plutons and relative to an interpreted Miocene surface. (For interpretation of the references to color in this figure legend, the reader is referred to the Web version of this article.)

the same thin section (Fig. 7A). Observations of this ductile dynamic recrystallization show similar top-(down-)west kinematics. Therefore, we interpret these samples show brittle fracturing overprinted with crystal-plastic deformation with the same shear kinematics. This transition may be driven by different temperatures or strain rates of deformation, or variable impacts of fluids.

The fundamental observation of crystal-plastic dynamic recrystallization overprinting brittle fractures has four potential explanations. First, the samples could have experienced a prograde path where they first experienced brittle cataclasis and as temperatures increased, crystal-plastic deformation mechanisms activated. This scenario is perhaps least likely for the study area, given the geologic history suggests extension and strain started shortly after plutonism and heating (Faulds et al., 2002b; Zuza et al., 2019) and thus it is unlikely that brittle shear zones formed here before higher temperature deformation. Furthermore, our interpreted kinematic and thermal history suggests that brittle deformation mechanisms would have overprinted ductile deformation during progressive cooling and exhumation.

Second is a model where the general temperature-strain regime was one that promoted crystal-plastic deformation, but there was coeval brittle failure on overlapping spatial and temporal scales, such as high stress coseismic rupture that propagated down from the overlying brittle crust (e.g., Chatzaras et al., 2020). Although speculative, the kinematic similarity between brittle and ductile deformation suggests that these two deformation mechanisms operated at similar times.

Third, progressive shearing may have occurred at the broad temperature range spanning brittle vs ductile feldspar deformation, and the variable cycling between deformation mechanisms occurred due to minor variations in temperature, composition, and strain rate (e.g., Gottardi and Hughes, 2022). For example, increased pore-fluid pressures could have promoted fracturing (Etheridge, 1983; Etheridge et al., 1984; Sibson, 1977) on punctuated timescales.

Fourth, the thermal structure of the crust may have varied through time during progressive plutonism. The Aztec Wash pluton (i.e., 15.7

Ma; Faulkner et al., 1995) was emplaced slightly after the Searchlight pluton, and it is possible that an already cooled, embrittled shear zone in the Ireteba pluton was re-heated during the emplacement of the Aztec Wash pluton. In these last three end-member scenarios, brittle fractures would have been subsequently overprinted by crystal-plastic deformation.

Fluids may have impacted deformation in these samples in several ways, including chemically driven neocrystallization (Stünitz and Fitz Gerald, 1993), enhanced grain-boundary mobility to promote grain boundary migration (Mancktelow and Pennacchioni, 2004; Urai et al., 1986), and increased pore-fluid pressure to drive fracturing (e.g., Etheridge, 1983; Etheridge et al., 1984; Sibson, 1977). Evidence for fluid activity may include (1) a compositional change of the recrystallized feldspar grains, (2) a related development of myrmekite, (3) evidence for hydrous phases as secondary minerals, (4) reprecipitation of new grains within pressure shadows (Simpson and Wintsch, 1989), and/or (5) enhanced dynamic recrystallization or grainsize reduction near potential fluid pathways.

It is impossible decipher the exact role fluids played in the observed samples, but we can offer limited interpretations. Myrmekite and hydrous phases are absent across much of the deformed Ireteba pluton samples, and we interpret that fluids were not pervasive throughout the deformation history. Chlorite and albitization occurred along late-stage cracks that cut across deformation fabrics and recrystallized grains (Fig. 10). We interpret that fluid-assisted replacement of K-feldspar by albitic plagioclase may have been a late-stage process that exploited high-permeability crack networks. Furthermore, because the fine-grained phases in the ultramylonite had similar compositions to the protolith feldspars (Fig. 10D), we suggest that the main deformation and grain-size reduction mechanisms were not dissolution/reprecipitation or neocrystallization, which is expected to result in compositional variations (Stünitz and Fitz Gerald, 1993). However, plagioclase in the R′ shear zone was significantly more albitic than the adjacent relict plagioclase (Fig. 10). This suggests that either neocrystallization operated locally during fluid-present deformation or this recrystallized R′ shear zone experienced albitization at a late stage due to its higher permeability. Most of the recrystallized grains in the R′ shear zone were K-feldspar, which did not display any compositional variations from the relict prophyroclasts. All of these observations suggest that fluid played a limited role in the investigated samples. Subgrain rotation recrystallization does appear enhanced near the R' shear fractures (Fig. 7E–F), which suggests fluids within the shear zones may have aided in dynamic recrystallization of the relict grains.

Feldspar phases within the ultramylonite zones displayed a distinct lack of CPO, whereas quartz had a moderate CPO. Plotting M and R indices from feldspar phases for our analyzed EBSD maps for samples 19SNV23 and 19SNV24a shows how the transition from protomylonite to ultramylonite leads to more random fabrics (Fig. 12) (data in Supplemental Table S1). This relationship suggests that dislocation creep is not the dominant deformation mechanism in the ultramylonite shear zones, because this mechanism should develop a CPO. Therefore, we interpret that the weak/absent CPO, very small grain-size, four-way straight grain boundaries demonstrate grain-boundary sliding diffusion creep in the ultramylonite shear zones (Ashby and Verrall, 1973; White, 1977, 1979). In particular, CPO weakening can be driven by diffusion creep (Bestmann and Prior, 2003; Jiang et al., 2000), cataclastic flow, or chemically driven neocrystallization (Stünitz and Fitz Gerald, 1993). These mechanisms may have acted simultaneously, potentially overprinting each other, in the finite strain record, but we argue that diffusion creep is the main mechanism that was observed in the mylonite zone. This is because the relatively uniform grain-size and lack of angular grains in the ultramylonite zones (e.g., Figs. 7I and 8D) are inconsistent with cataclastic flow as the primary deformation mechanism (e.g., Figs. 7I and 8D) and the lack of compositional changes between protolith feldspars and the recrystallized grains is evidence against significant neocrystallization (Fig. 10).

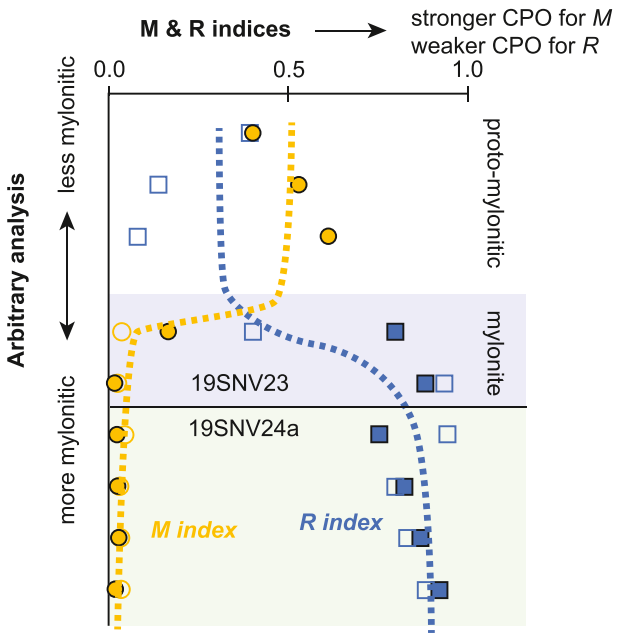

Fig. 12. Plot of M- and R-indices from analyzed samples in diffuse brittle-ductile transition zone, highlighting how CPO strength measured through both proxies decreases with mylonitzation and grain-size reduction (data in Supplemental Table S1).

The dynamic recrystallization of the R and R′ shears involved dislocation creep mechanisms because a moderate CPO was observed. The increased subgrain density within the porphyroclasts toward the recrystallized R or R′ shear zones (Fig. 7F–H) can either be interpreted to indicate that progressive subgrain formation led to the reduced grain-size observed in the recrystallized R-R′ shear zones or that subgrain rotation recrystallization was locally enhanced near these shear zones and grain boundaries. The mean subgrain size of ~20 μm in the coarse K-feldspar (Fig. 7E–G) broadly overlaps the ~18 μm recrystallized grain size in the R' shear zone (Fig. 7H). However, these observed grain-sizes are significantly larger than grains in the ultramylonite zone (i.e., <10 μm; Figs. 7I and 8D), which suggests another grain-size reduction mechanism is required to explain the fine <10 μm grain size.

The exact process of grain-size reduction and resulting strain localization in feldspar-dominated rocks remains unclear and widely discussed. Grain-size reduction may proceed via metamorphic reactions and dissolution-reprecipitation (Stünitz and Fitz Gerald, 1993; e.g., Fukuda et al., 2012; Gueydan et al., 2003, 2003; Oliot et al., 2010; Tsurumi et al., 2003), dislocation creep and dynamic recrystallization (Svahnberg and Piazolo, 2010; Tullis and Yund, 1985), brittle fracturing and cataclasis (Negrini et al., 2014; Ree et al., 2005; Tullis and Yund, 1987), and/or a combination of mechanisms (Mancktelow and Pennacchioni, 2004; Ree et al., 2005; Sullivan et al., 2013). There is a simultaneous competition between brittle, ductile, and reaction-based grain-size reduction and deformation mechanisms that is controlled by a function of temperature and stress, and thus grain-size reduction is not a monotonic process but varies during the evolution of a shear zone (De Bresser et al., 1998; Platt and Behr, 2011). The mechanisms of grain-size reduction in the observed samples are important for understanding the transition to strain weakening via grain-size-sensitive diffusion creep, a process that does not reduce grain size.

Although albitization observed in sample 19SNV23 suggests that dissolution-reprecipitation operated locally (Fig. 10), we do not think this process was the main driver of grain-size reduction in the mylonitic shear zones. Specific evidence against this mechanism is that the composition of the finest grains is the same as the relict larger grains (cf. Marti et al., 2018; Wintsch and Yi, 2002) (Fig. 7A), no myrmekite was

observed (Dong et al., 2019), and there was no observation of asymmetric dissolved and reprecipitated grains, especially with any contact relationships with larger, possibly dissolved grains.

We interpret that combined dislocation creep and cataclastic flow was primarily responsible for the significant grain-size reduction observed in the ultramylonite samples. Feldspar grains are heavily fractured and disaggregated along the 19SNV24d through 19SNV24a traverse, which demonstrates how brittle fracturing and cataclastic flow leads to significant grain-size reduction in these samples (Fig. 6D–G). However, frictional sliding interpreted in sample 19SNV23 based on the linear R and R′ fractures does not show evidence for brecciation or heterogeneous grain-sizes that might be characteristic of cataclastic flow (Fig. 7C). The interlocking grains (Fig. 7H) and moderate CPO (Fig. 7D) lead us to interpret that these shear zones were dynamically recrystallized after brittle failure. The observation of subgrain development within the larger K-feldpsar grains, with increasing density toward the grain boundary (Fig. 7E–G), further reveals the importance of dislocation creep as a grain-size-reduction mechanism. The ~20 μm subgrains are essentially the same size as the ~18 μm grains observed in the adjacent R' shear zone. In this case, we interpret that combined cataclasis and overprinting dislocation creep was responsible for developing the fine grains.

Tullis and Yund (1987, 1992) discuss how cataclastic flow occurs within feldspars over a wide range of temperatures to promote grain-size reduction that transitions to other mechanisms of crystal-plastic deformation, such as dislocation or diffusion creep. Here we have observed this process in the transition from a protomylonite to ultramylonite in a single sample (Fig. 7) and across an outcrop scale transition to an ultramylonite zone (Fig. 6). Overprinting brittle cataclasis and disclocation creep can lead to strong grain-size reduction at relatively strong BDT depths.

We cannot rule out the role that fluids played in this process. Some observed albitization suggests that dissolution-reprecipitation occurred, at least at local scales, and the neocrystallization can generate fine grainsizes with no CPO. We envision that at the base of the seismogenic crust, fluids may have assisted fracturing via increased pore-fluid pressure and with enhanced permeability, the neocrystallization process may have generated small recrystallized feldspar grains with no CPO. This mechanism would have operated in conjunction with the aforementioned cataclastic and crystal-plastic deformation.

5.2. Interpretations of the ZHe thermochronology data

The three ZHe thermochronology traverses sampled mid-Miocene plutons (Fig. 11). If the ZHe data record conductive cooling of these plutons to background ambient temperatures, one would expect a potential decoupling between ZHe ages above and below the approximate PRZ depth. This is because that the uppermost parts of the pluton would sit above the PRZ depth and cool down through the closure temperature quickly, whereas the lower parts of the pluton likely resided at deeper levels than the PRZ depth (i.e., ambient temperatures greater than ZHe closure temperatures) maintaining an open ZHe system until exhumation. Therefore, those samples above would be slightly younger than the intrusion age and those below the PRZ should potentially be much younger, recording some later phase of exhumation. However, our results show similar ZHe ages above and below the PRZ (Fig. 11), which broadly implies a fast cooling that could have resulted from the extension-related exhumation. Therefore, the new ZHe data constrains ca. 13–15 Ma exhumation related regional extension at this time. Coupled conductive and advective heat transport led to rapid cooling from pluton-intrusion temperatures (>700 °C) to ~200 °C in 1–2 Myr. Most relevant to this study, we know that the crust here at ~10 km paleo-structural depth (~300 °C ambient temperatures) prior to tectonic exhumation cooled to below 200 °C by 14 Ma. The Late Cretaceous Ireteba pluton samples from this study were surrounded by Miocene plutons, and thus we establish that these temperature constraints are maxima.

Numerous ZHe aliquots yielded anomalously young ca. 11 Ma ages, which we interpret to reflect heating from overlying volcanic rocks (Fig. 13A), including the shallowly dipping ca. 11.3 Ma basalt flows mapped in the study area (e.g., Faulds et al., 2001; Hinz et al., 2012) (Tb in Fig. 4). This interpretation implies that the plutons were tilted as coherent bodies, given the general inverse correlation of ZHe age vs structural depth (Fig. 11), after which subhorizontal ca. 11.3 Ma basalt flows were deposited over the Dupont Mountain hanging wall and footwall rocks (Fig. 13A). This would have thermally perturbed the He systematics in nearby underlying samples. Subsequent high-angle normal faulting reorganized the system, such as dropping part of the Dupont Mountain fault hanging wall down-to-the-west against its underlying footwall, around the location of sample 18SL8 (Fig. 13A). Confirmation of this process is that sample 18SL8 in the hanging wall of this high-angle normal fault preserves a record of thermal perturbation from the ca. 11.3 Ma basalt, whereas sample SLP1 in the footwall of this fault does not (Fig. 11). Later tapered incision of the Colorado River east of the study area mostly removed rocks that were thermally influenced by the 11.3 Ma basalt, thus explaining why most samples did not record ca. 11 Ma ages, except (1) at the structurally highest and further west samples (18SL10) that would have been least incised by Colorado River erosion and (2) the faulted 18SL8 sample.

To test this hypothesis, we conducted forward thermal history models using HeFTy (Ketcham, 2005) for the Searchlight pluton dataset. We assume eU is a proxy for total accumulated radiation damage, and leverage the relationship that grains with different amounts of radiation damage are reset to varying degrees during a reheating event (Guenthner et al., 2013). The modeled t-T path included basic elements of the inferred geologic history (Supplemental Materials) including high temperatures during pluton emplacement at 16 Ma, rapid cooling to the near surface by 14 or 16 Ma, and residence at near surface conditions where the rocks would have been thermally affected by overlying volcanic rocks. We conducted two forward models: one assumed rapid cooling to near-surface temperature by 14 Ma and the other by 16 Ma (Fig. 13B), which can reflect structurally lower and higher positions respectively, within the rotating and cooling Searchlight pluton (Fig. 13B). The models employed a rapid 100 year reheating event at 11.3 Ma to peak temperatures between 140 and 300 °C (Fig. 13B) to predict zircon He dates for the full range of eU values. Additional model parameters are detailed in the Supplemental Material following the reporting protocol of Flowers et al. (2015).

The forward model predicted ZHe date patterns show a positive trend between date and eU (**Fig, 13C, D**). The slope is dependent on the 11.3 Ma reheating temperature, with lower reheating temperatures having a steep slope at low eU followed by nearly flat trends, and higher reheating temperatures having a shallower slope with younger dates across a wider range of eU (**Fig, 13C, D**). For example, the 140 °C reheating only minorly affects grains with low eU (<50 ppm), whereas the 300 °C reheating affects the measured dates at the full range of modeled eU (0–1200 ppm). The positive date-eU trend is consistent with expected trends given the samples' thermal history (i.e., radiation damage accumulation is relatively low, and the sample experienced a relatively rapid thermal pulse), with the lower eU grains being the most affected (Guenthner et al., 2013). The model predicted dates are consistent with the observed data patterns for the Searchlight pluton, capturing the mild positive date-eU relationship and the full range of observed dates. Importantly, the forward models and our dataset show that a 100 year duration basalt reheating at ca. 11.3 Ma could have led to resetting or partial resetting of the ZHe ages dates, including the ~11 Ma observe dates (Fig. 13C and D). We envision that the Spirit Mountain Batholith samples to the south was similarly influenced by the ca. 11.3 reheating, reflected in some individual ca. 11 Ma aliquot ages (Fig. 11D).

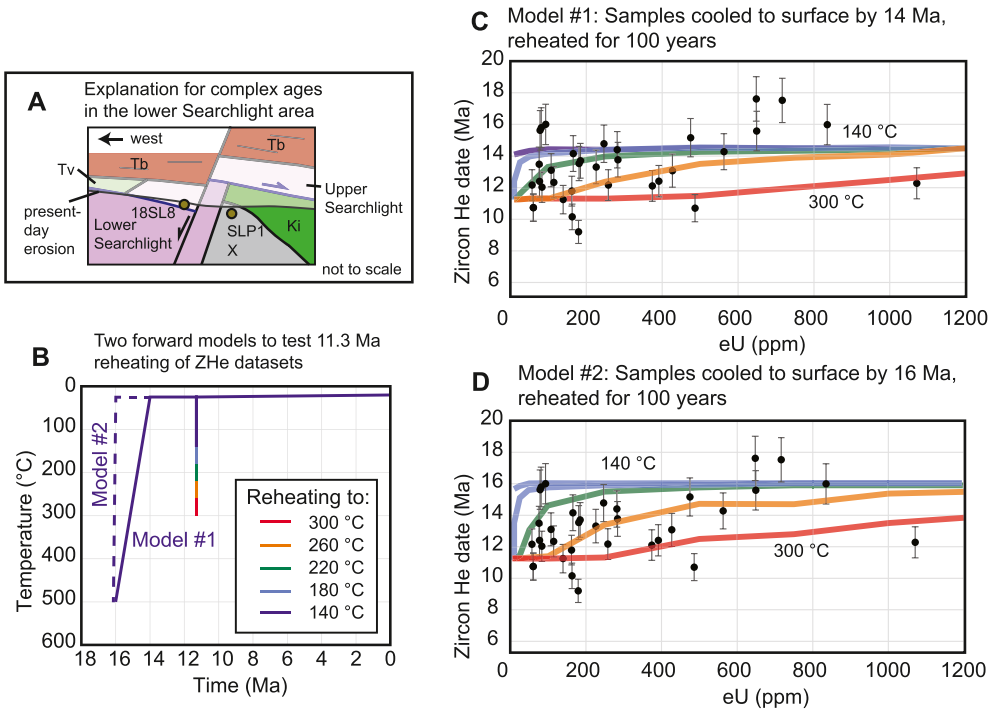

Fig. 13. (A) Sketch of inferred relationship to explain ages of Searchlight ZHe samples 18SL8 and SLP1 in the context of Dupont Mountain fault, overlying ca. 11.3 Ma basalt flows (Tb), and later high-angle normal faulting. Mapping by Hinz et al. (2012) shows that sample 18SL8 was in the upper plate of the Dupont Mountain fault, dropped downward by a significant west-dipping high-angle normal fault. This may explain the similarity of ZHe dates between 18SL10 and 18SL8. (B–C) HeFTy forward modeling to test whether heating of an overlying basalt flow could reset ZHe dates for the Searchlight pluton traverse. (B) Two temperature-time histories: model #1 involves slower cooling from 500 °C to surface temperatures by 14 Ma whereas model #2 involves more rapid cooling to surface temperatures by 16 Ma. Both invoke a pulse of heating at ca. 11.3 Ma for 100 years, with varying maximum temperatures (see colored lines). (C) Results for model #1 and (D) model #2 plotted in ZHe data-eU space for different maximum temperatures along with individual datapoints for the Searchlight data. The overlap of datapoints and forward-model results demonstrates that the overlying basalt could have reset some of the ZHe aliquots.

5.3. *Thermal and kinematic constraints*

With deformation and thermal conditions, we aimed to construct a reasonable deformation mechanism map. We first evaluate a representative strain rate. Regionally, strain rates probably peaked at ~10^{-13} s^{-1} (Gans and Bohrson, 1998). We validate this estimate for our local geologic setting through simple geometric and kinematic arguments. The Searchlight pluton tilted 90° on its side, and thus in 2D it rotated ¼ of a complete circle. Therefore, the 2D shear strain is approximately ¼ of a the circumference of the rotating shear zone ($\frac{\pi r}{2}$), divided by the radius of rotation (r), so that shear strain equals $\frac{\pi}{2}$ and strain rate $\frac{\pi}{2t}$ (e.g., Zuza et al., 2019). Rapid deformation persisted for ca. 0.5 Myr (Faulds et al., 2001; Zuza et al., 2019) and thus the strain rate was ~10^{-13} s^{-1}. This rate assumes the strain was accommodated across the entire rotating section, but given that strain was less in the upper brittle part of the pluton and probably localized on 0.1–1.0 m shear zones, we may speculatively assume that strain rates were one or two orders of magnitude faster, perhaps closer to ~10^{-11} s^{-1}.

There are no quantitative temperature constraints for deformation discussed in this study. Dynamic recrystallization of feldspar, particularly via SGR, implies temperatures >500 °C (e.g., Tsurumi et al., 2003; Tullis and Yund, 1991, 1985). To further evaluate temperature conditions, we used knowledge of the geologic history to construct a simple 1D cooling model to estimate the temperature history. The coupled Ireteba-Searchlight plutons started to deform, extend, and rotate shortly after intrusion of the Searchlight pluton at 16.2 Ma (e.g., Faulds et al., 2001), with fast rotation lasting only ~0.5 Myr as supported by tilted dikes, tilted volcanic rocks, thermochronology, and paleomagnetic data

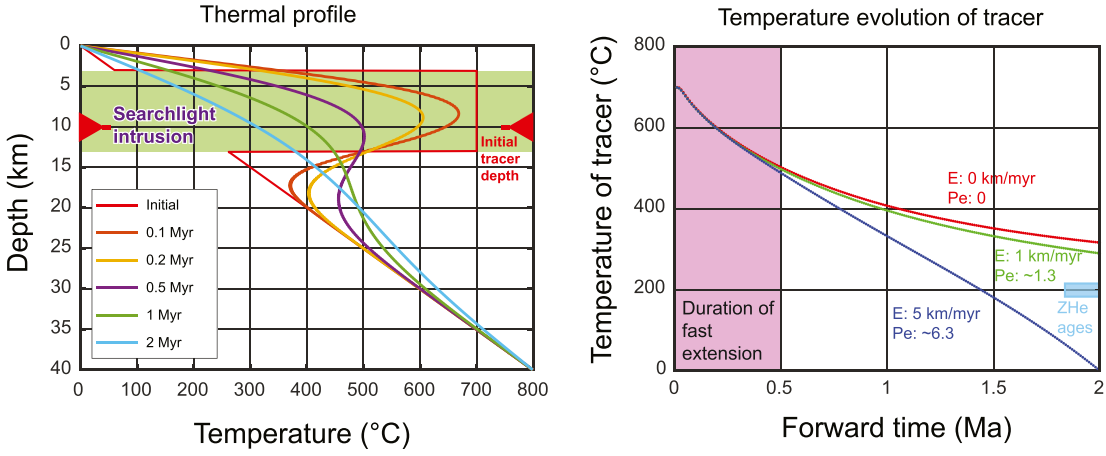

Fig. 14. Thermal model used to constrain deformation temperatures near the BDT as a function of time. (A) Temperature profile assuming no exhumation and (B) plot of temperature evolution of a tracer at variable exhumation rates. Deformation is assumed to have commenced immediately after the intrusion of the Miocene Searchlight pluton, with most strain occurring within 0.5 Myr. Model assumes intrusion at 3–13 km depth at 700 °C into crust with an initial geothermal gradient of 20 °C/km. Tracer starts at ~10 km model depth and the system experiences exhumation at rates (E) of 0, 1, and 5 km/myr. Also plotted are constraints from the zircon helium thermochronology (ZHe) that suggest the exposed rock was ~200 °C by ca. 14 Ma (Fig. 4). Pe–Péclet number.

(e.g., Faulds et al., 2001, 2002a; Zuza et al., 2019). Therefore, deformation observed in the Ireteba pluton occurred within ~0.5 Myr of the Searchlight pluton intrusion, and we can thus model the thermal history imparted by the proximal Searchlight pluton from 16.2 Ma to 15.7 Ma.

We construct a crustal column of the Ireteba pluton with a steady-state temperature gradient from 0 °C at the surface to 800 °C at 40 km depth. We modeled the Searchlight pluton intrusion with a 700 °C thermal pulse spanning paleo-depths of 3–13 km (i.e., 10 km tall to match map- and cross-section observations) (Fig. 14), which is slightly colder than the 750–830 °C pluton-temperature estimates (Bachl et al., 2001) because we are attempting to model the adjacent Ireteba pluton. The model cools conductively with an advective/erosive component using the Péclet number (*Pe*) and exhumation (*E*) (e.g., Cao et al., 2019; Zuza et al., 2019). The 1D cooling follows the following relationship:

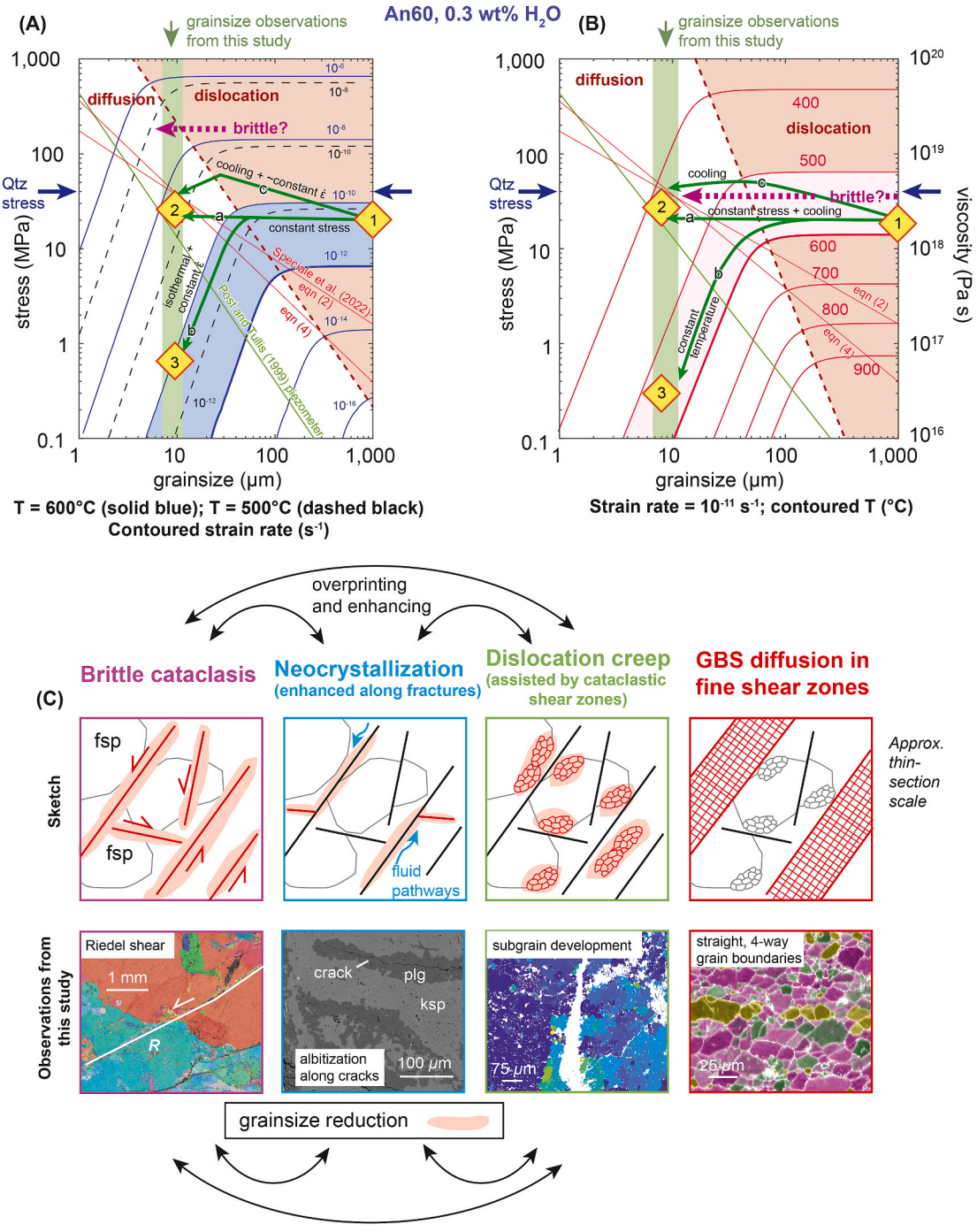

Fig. 15. Deformation mechanism maps for the feldspar mylonites at (A) constant temperature or (B) constant strain rate, with envisioned grain-size versus stress evolution. Shaded fields represent inferred constraints for the shear zones. Three feldspar grain-size piezometers are plotted. Purple brittle curves schematically show grainsize reduction, but are not modeled in these maps. See text for interpretative explanation. (C) Progressive, overprinting deformation mechanisms active in the Ireteba shear zones drafted schematically (top) and relevant examples from this study (bottom). Grain-size reduction occurs during brittle cataclasis, dislocation creep (subgrain rotation), and more limited neocrystallization, which ultimately allows for grain-boundary sliding (GBS) to operate at very fine grain-sizes. fsp–feldspar; ksp–K-feldspar; plg–plagioclase; qtz–quartz (For interpretation of the references to color in this figure legend, the reader is referred to the Web version of this article.)

$$\rho C_p\left(\frac{\partial T}{\partial t}-\frac{\partial T}{\partial z}\cdot E\right)=\lambda\frac{\partial^2 T}{\partial x^2} \quad (1)$$

where T is the temperature at depth z, t is time, ρ is density, C_p is the heat capacity of rock, and λ is the thermal conductivity of rock. Pe is the ratio between timescales of conduction versus advection:

$$Pe=\frac{EL}{\kappa} \quad (2)$$

where L is the lengthscale of our analysis and κ is thermal diffusivity. Given $\rho = 2.7$ g/cm^3, and $\kappa = 10^{-6}$ m^2 s^{-1}, we tracked the temperature-time evolution of a parcel of rock that started at ~10 km paleo depth and experienced exhumation rates of 0, 1, or 5 km/myr, which equates to Pe of 0, ~1.3, or ~6.3 respectively (Fig. 14).

Our thermal model suggests that shear zones at ~10-km paleo-depth would have developed at temperatures of ~600-500 °C over the first 0.5 Myr (Fig. 14), which matches qualitative deformation temperatures observed in our microstructural analyses. Based on the interpreted geologic history of the region, we know that these elevated temperatures cooled rapidly through time, probably back down to ~400 °C or less within 0.5 Myr. ZHe data requires most of these rocks to cool below ~200 °C by ca. 14 Ma (i.e., ~2 Myr in the forward model) (Figs. 11 and 14). Limitations of this model include uncertainty in the age of the intrusion, uncertainty in the age of the shear zones, and the fact that the model attempts to describe the approximate temperature range of the deforming crust near the Searchlight pluton. That said, our observations and this model suggest similar temperature and timing constraints for the studied shear zones.

5.4. Deformation history from the thin section to deformation mechanism map

Deformation mechanism maps were constructed following the procedures of Rybacki and Dresen (2004). Experimental flow law parameters for feldspar are sparse, and our analyzed samples contained sodic plagioclase and K-feldspar, which do not have experimental data. That said, we chose to use the parameters for An60 plagioclase (0.3 wt% H_2O) (Dimanov et al., unpublished, cited in Rybacki and Dresen, 2004). Deformation of K-feldspar and plagioclase may operate similarly (e.g., Stünitz and Fitz Gerald, 1993; Kilian et al., 2011), but we urge caution in interpreting results drawn from these deformation mechanism maps based on slightly different rock types.

Deformation mechanism maps were constructed for both a constant temperature and a constant strain rate (Fig. 15A and B), using knowledge of deformation conditions developed in this study. That includes deformation temperatures of 500–600 °C and shear-zone strain rates of 10^{-11} s^{-1}. Also plotted on these maps are the paleopiezometers (Post and Tullis, 1999; Speciale et al., 2022) (red lines), and the range of fine-grained recrystallized grain-sizes observed in the ultramylonite shear zones (~7–10 μm).

Here we relate knowledge of the geologic history with deformation mechanism maps (Fig. 15A and B) and thin-section observations (Fig. 15C) to describe deformation observed in samples 19SNV24A and 19SNV23. We start with the knowledge that Ireteba grain-size started at >1 cm, which is not shown in the maps. Starting at ca. 16.2 Ma, Searchlight pluton intruded the system and regional extension initiated, thus driving flow of the Dupont-Mountain footwall rocks, including the Ireteba pluton, to the surface. We assume this heated the studied rocks to ~600 °C. The exact path of the shear zone through deformation-mechanism space depends on the strain rate, temperature, and grain-size evolution. Dislocation creep would have started near the diamond labelled "1", including SGR perhaps facilitated by fracture pathways and fluid flow, reducing the grain-size at relatively constant strain rates and temperatures (Fig. 15). Note, as outlined in this study, dislocation creep alone cannot reduce the grain-size to the observed ≤10 μm conditions and therefore cataclastic flow during brittle fracturing may have caused the additional necessary grain-size reduction, which is shown schematically with a dashed purple line at faster strain rates (e.g., Fagereng and Biggs, 2019) (Fig. 15). Fluid-assisted neocrystallization with fluids concentrated in fracture networks could have also reduced the grainsize (Stünitz and Fitz Gerald, 1993), parallel to the brittle cataclastic vector. We emphasize brittle failure, cataclastic flow, and neocrystallization are not directly modeled in these maps. We envision that cycles of brittle failure, fluid flow with potentially increased pore-fluid pressure, and dislocation creep impacted these shear zones, causing dynamic recrystallization of the brittle Riedel shear networks (Fig. 15C).

In Fig. 15A we show three possible paths with fixed temperature conditions. First, assuming constant stress and temperature conditions (Platt and Behr, 2011), grain-size reduction may have progressed via dislocation creep mechanisms that will shift the grain size towards the piezometry line bringing rocks to grain-size of ≤100 μm (path "a" from "1" toward "2"). If we assume the constant stress condition, the shear zone width will also remain constant but deformation will occur at a transient, faster rate condition signifying rheological weakening (Platt and Behr, 2011). This trajectory intersects the observed grain-size conditions and feldspar piezometers at diamond "2" (Fig. 15A). Once at the diamond "2" position, the rock is within the diffusion creep region, where grain size correlates with stress.

To comply with a constant strain rate condition (10^{-11} s^{-1}), the shear zone follows the 10^{-11} s^{-1} strain rate curve (path "b") to reach the lower strength condition (<1 MPa) (diamond "3"). From positions "2" to "3", rheological weakening is achieved by the reduction of the strength (and viscosity) of the shear zone. De Bresser et al. (1998) suggested that in this scenario, grain growth may occur to move the deforming rock toward the diffusion-dislocation boundary. Alternatively, if we assume a constant strain rate associated with cooling deformation temperatures, path "c" moves up and left (black dashed lines are strain rate contours at ~500 °C) to reflect the cooling-induced strength increase (Fig. 15A). This path may have peaked at ~40 MPa based on observed quartz stress conditions and then experienced a stress drop toward ~20–30 MPa to intercept the piezometer lines.

These paths can alternatively be viewed in a constant strain rate map (Fig. 15B). Constant stress (Platt and Behr, 2011) and strain rate conditions would project the rock through the dislocation creep regime (path "a") toward diamond "2" in the diffusion creep regime. Syn-kinematic cooling (to ~450 °C) at fine grain-sizes in the diffusion creep field would move the rock toward the piezometer lines. This implies that the strength increase associated with decreasing temperatures is counteracted by the rheological weakening caused by grainsize reduction in the diffusion creep regime to remain at a constant stress state. A constant strain rate and temperature path (path "b") would lead to a dramatic stress drop toward diamond "3". Alternatively, syn-kinematic cooling throughout the dislocation creep regime would lead to increased strength (and viscosity) toward the ~40 MPa quartz-based stress conditions with a minor stress drop to the feldspar piezometer lines (path "c") (Fig. 15B).

Although described as discrete paths, it is likely that the shear zone evolved as a hybrid between these options. Given our constraints of a cooling system, we would speculatively favor paths drafted in the constant strain rate maps (Fig. 15B), which show our envisioned progression from hot (~600 °C) temperatures to colder (~400 °C) conditions during progressive deformation along paths "a" and "c", but we acknowledge that reality probably involved combined effects in each map.

Our observations and deformation mechanism maps suggest that this feldspar-dominated shear zones deformed at stresses of ≤50 MPa. Some of our quartz piezometer relationships suggest broadly similar stresses of ~40 MPa. Within uncertainties and natural variability, these stress estimates overlap. Interestingly, they are all significantly lower than other estimates for peak stress near BDT conditions. For example, naturally exhumed BDTs in quartz-rich rocks exhibit dislocation creep deformation mechanisms and peak strengths of ≥150 MPa (Behr and Platt, 2011,

2014; Kidder et al., 2012; Zuza et al., 2022a, 2022b). The ultramylonite zone with a small grain size indicates the strength in the shear zone could be as low as 0.1–1 MPa if the grain size does not grow toward the diffusion-dislocation boundary. This highlights the relative weakness of feldspar-rich, relatively hot crustal shear zones that deform via diffusion-creep mechanisms (Kenkmann and Dresen, 2002; Montési and Hirth, 2003). Furthermore, partitioning of shear motion into numerous local shear zones can lead to lower strain rate and flow stress in each individual shear zone (Platt and Behr, 2011).

We interpret that severe grain-size reduction via cataclastic flow, local fluid-assisted neocrystallization, and overprinting dislocation creep (Tullis and Yund, 1987) was a substantial strain weakening process to enable grain-size-sensitive diffusion creep in these feldspar-rich shear zones (Fig. 15C). Therefore, under certain deformation conditions, feldspar-dominated lithologies may be potentially weaker than quartz (Menegon et al., 2008), thus resulting in strain localization during tectonic deformation (Olsen and Kohlstedt, 1984; Platt, 2015; Viegas et al., 2016; Warren and Hirth, 2006). This collective process appears most viable at or just below BDT depths, where the aforementioned grain-size reduction mechanisms are operative (e.g., cataclasis and neocrystallization). At hotter, deeper depths, even if grain size is reduced enough to initiate diffusion creep, grain growth may occur driven by surface energy in the absence of grain-size reduction mechanisms (De Bresser et al., 1998; Platt and Behr, 2011), moving the shear zone back toward the diffusion-dislocation creep boundary. Therefore, our study suggests that mid-crustal BDT depths may be particularly susceptible to initiating grain-size-sensitive diffusion creep deformation, allowing the mid-crust to be relatively weaker than the hotter lower crust. Conversely, our interpretations suggest that it is more difficult to initiate diffusion-creep deformation for structurally deeper, lower crust shear zones devoid of brittle failure or fluid-mediated neocrystallization that cause substantial grain-size reduction. At such depths, dislocation creep deformation mechanism will persist, where viscosity and strength are most dependent on temperature (Fig. 15B) and potential partial melting. For example, the structurally deeper and hotter lower Ireteba pluton (Fig. 9) did not experience cataclasis and sufficient grain-size reduction to activate diffusion creep.

Postseismic, interseismic, lake-shore rebound, and topographic analyses have been used to suggest lower crust viscosities as low as 10^{18}–10^{19} Pa s (Clark and Royden, 2000; Shi et al., 2015; Zhao et al., 2017). Although these viscosities are attainable for quartz-dominated lithologies (Schutt et al., 2018) or mixed-phase systems where rheology is governed by the weaker quartz phase, these values are difficult to reconcile for feldspar-rich lithologies at reasonable lower crust temperatures and moderate bulk strain rates (~10^{-14} to 10^{-16} s^{-1}), assuming dislocation creep (Rybacki and Dresen, 2000, 2004; Schutt et al., 2018) (Fig. 1). However, if grain size can be adequately reduced, it is possible for diffusion creep to activate with discrete shear zones deforming at moderate 500–600 °C temperatures and viscosities of ~10^{18} Pa s at very fast strain rates (e.g., 10^{-11} s^{-1}) (Fig. 15B) or viscosities of ~10^{20} Pa s at more moderate rates (e.g., 10^{-15} s^{-1}) (Fig. 15B). This logic provides a mechanism for low viscosity deformation of feldspar-rich crust. However, at such temperature conditions, there is a competition with resultant grain growth (De Bresser et al., 1998; Platt and Behr, 2011), and continued diffusion creep would require grain-size reducing processes. This caveat may complicate models for low viscosity values in the lower crust, in the absence of fluid-induced weakening (Hirth and Kohlstedt, 1996) or partial melting. Paradoxically, regions of the middle crust just at or below the BDT that experience grain-size reducing cataclasis and fluid-mediated neocrystallization may be relatively weak due to the activation of diffusion creep deformation compared to the hotter, lower crust where dislocation creep dominates. This may support the existence of confined low-viscosity horizons or channels (e.g., Clark and Royden, 2000) without partial melts or fluids.

5.5. Coexisting and overprinting brittle-ductile structures

At paleo-BDT depths we observed coexisting brittle and ductile structures, which may require a unique geologic history and tectonic setting. Our envisioned geologic history does not readily support a simple prograde deformation model, where brittle fracturing is overprinted by crystal-plastic deformation during heating and burial. We can envision two distinct scenarios to track a parcel of rock that originated at ~10 km *T-t* history (Fig. 16). In Path 1, the parcel cools conductively after Ireteba intrusion to temperatures below BDT conditions. At ca. 16 Ma, with the intrusion of the Searchlight pluton, the rock is heated to above feldspar and quartz BDT conditions. Without faulting, this parcel cools conductively, slowly through the temperature windows for feldspar and quartz plasticity back toward the ambient geotherm conditions. This scenario predicts a long window for ductile structures to develop, which should thus (1) destroy any earlier brittle structures and (2) show a more limited range of deformation temperatures during progressive cooling. Hypothetical Path 2 deviates from Path 1 in that footwall exhumation of the Dupont Mountain fault promotes rapid advection and faster cooling. Therefore, the parcel spends much less time in the ductile feldspar and quartz regimes as it cools rapidly toward the observed ZHe *T-t* constraints. This path allows preservations of both ductile and brittle structures by essentially quenching them over a short timeframe and limited finite strain.

Our observations are consistent with Path 2, which may explain why a range of brittle to ductile-feldspar conditions were observed. During rapid cooling and footwall rotation (Fig. 3), the BDT would migrate to structurally deeper levels, progressively freezing ductile fabrics in the brittle crust. Conversely, the structurally deeper parts of the Ireteba pluton shows a restricted range of ductile deformation conditions, which may reflect prolonged residence at hotter temperatures.

5.6. Implications for Miocene extension in the Colorado River Extensional Corridor

Field observations from across the Ireteba pluton are consistent with it being tilted westward on its side, with western exposures displaying brittle deformation features and eastern exposures showing strongly lineated and sheared rocks (Fig. 4). This matches observations from the Searchlight pluton just south of the Ireteba pluton consistent with westward rotation in the footwall of the east-directed Dupont Mountain fault (Bachl et al., 2001; Faulds et al., 2001; Zuza et al., 2019). This

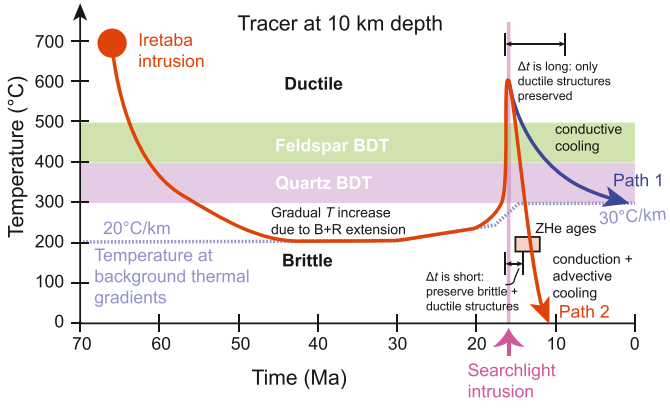

Fig. 16. Sketch of temperature vs time (*t*) history of the Ireteba pluton, demonstrating why this system uniquely recorded brittle and ductile structural features. Rapid heating and cooling caused Δ*t* above quartz/feldspar crystal-plastic deformation temperatures to be brief, thus freezing brittle structures without substantial overprint (Path 2). Slower cooling and a longer Δ*t* would lead to overprinting of brittle structures, thus obscuring the history involving brittle cataclastic flow (Path 1). B+R–Basin and Range; BDT–brittle-ductile transition.

tilting is further validated by our new AlHbl pressure estimates that corroborate those of Bachl et al. (2001) (Fig. 4B), which together confirm that the tilted Searchlight pluton exposes rocks from paleo-depths of ~12 km–~4 km. Such footwall tilting appears to be important for deformation in the CREC (e.g., Gans and Gentry, 2016), although because many detachment-fault systems consist of heterogenous footwall rocks consisting of polyphase-deformed Proterozoic gneiss, quantifying the degree of Miocene tilting versus earlier deformation can be ambiguous. In this sense, the tilted Miocene plutons in the CREC provide robust constraints on the degree and coherency of footwall tilting in this extension setting.

Shear zone observations across the Ireteba pluton show eastside up shear sense, similar to those observed in the Searchlight pluton (Zuza et al., 2019). Zuza et al. (2019) summarized several possible models for such top-west, bottom east shear, including hot footwall flow toward the Earth's surface, discrete imbrication, or pre-tilting subhorizontal top-west shear. Observations in this study do not uniquely address this question, but they provide constraints for interpretations of the eastside-up shear. Our traverse across the Ireteba pluton suggests that differences in deformation styles (i.e., from brittle to discrete shear zones to distributed ductile flow) reflect increased paleo-depths and temperatures, not discrete antithetic faults. This shear could reflect a pre-tilting subhorizontal shear zone (e.g., Singleton and Mosher, 2012), where mid-crust shear zones get captured by detachment faults, which is commonly interpreted in the CREC (e.g., Davis and Lister, 1988; Lister and Davis, 1989; Singleton and Mosher, 2012). Furthermore, a mid-crust top-west subhorizontal shear zone model would require a kinematic switch for the initiation of top-east Dupont Mountain faulting, which is structurally complex and unlike models of captured mid-crust shear zones (e.g., Davis and Lister, 1988; Lister and Davis, 1989).

ZHe thermochronology reveals rapid 15-14 Ma cooling at three transects along the Colorado River Extension Corridor (Fig. 11), clearly demonstrating that shortly after emplacement of the Spirit Mountain Batholith, Searchlight pluton, and Aztec Wash pluton, extension exhumed the footwall rocks. Similar timing constraints come from tilt fanning of overlying volcanic rocks, paleomagnetic data, and rotated dikes (Faulds et al., 2002b; Gans and Bohrson, 1998; Hinz et al., 2012; Zuza et al., 2019). Although there appears to be a northward younging trend to plutonism and extension, and ZHe data does not reveal any definitive trends, which may be due to the complex relationship between plutonism, conductive cooling, and footwall advection. Many single aliquots yielded ca. 11 Ma ages (Figs. 11 and 13) across a range of apparent structural depths, which is consistent with the plutons already being tilted on their side when thermally perturbed by shallowly dipping ca. 11 Ma volcanic rocks (Hinz et al., 2012).

6. Conclusions

Our coupled field, microstructure, and thermochronology study of a brittle-ductile transition across the Ireteba pluton provides new insights into strain localization in a feldspar-dominated lithology. This work shows that the footwall of the Dupont Mountain fault was tilted and exhumed rapidly after voluminous plutonism at ca. 15–17 Ma by east-directed Dupont Mountain faulting, which is tracked by zircon (U–Th)/He thermochronology and cooling to <200 °C by ca. 14 Ma. This exhumation led to a range of observed structural features across the west-tilted Ireteba pluton, including brittle deformation in the upper portions, mixed-mode brittle-ductile deformation in a transitional zone, and ductile flow-like conditions at depth.

At near BDT conditions, we observed discrete cm-scale fine-grained (7–10 μm grainsize) feldspar-rich ultramylonite shear zones, where the dominant deformation mechanism appears to have been diffusion creep. Observation of protomylonites adjacent to the ultramylonite zones shows that grain-size reduction was accomplished via overprinting brittle cataclasis, fluid-assisted fracturing and neocrystallization, and dislocation creep mechanisms. Our work demonstrates the importance of these strain weakening processes on localizing deformation in potentially strong feldspar-rich lithologies that may approximate mid-crust conditions to facilitate the development of grain-size-sensitive diffusion-creep shear zones. We suggest that this naturally deformed feldspar shear zone was preserved due to the unique geologic history with fast heating and exhumation, which froze both brittle and crystal plastic structures to provide valuable insights into mechanisms of feldspar deformation.

Data availability statement

Data used in this study can be found in the Supplemental Material, Supplemental Table, and geochron.org (http://www.geochron.org/results.php?pkey=38387), an online publicly accessible repository for thermochronology data.

Author statement

Andrew V. Zuza: Conceptualization, Methodology, Formal analysis, Investigation, Writing - Original Draft, Visualization, Supervision, Project administration, Funding acquisition **Wenrong Cao:** Conceptualization, Methodology, Investigation, Writing – Review & Editing, Supervision, Project, Funding acquisition **Angelica Rodriguez-Arriaga:** Investigation, Methodology, Formal analysis, Writing – Review & Editing **Joel DesOrmeau:** Methodology, Formal analysis, Investigation, Writing – Review & Editing **Margo Odlum:** Methodology, Formal analysis, Investigation, Writing – Review & Editing.

Declaration of competing interest

The authors declare the following financial interests/personal relationships which may be considered as potential competing interests:

Andrew V. Zuza and Wenrong Cao report financial support was provided by National Science Foundation.

Acknowledgements

This research was supported by the Tectonics Program of the National Science Foundation (EAR 1830139). We appreciate discussions in the field with Nick Hinz, Calvin Miller, Mike Eddy, Blair Schoene, Ayla Pamukcu, and Drew Levy. We appreciate editorial handling by Jianhua Li, and constructive comments by reviewers John Singleton, Nikki Seymour, and an anonymous reviewer.

Appendix A. Supplementary data

Supplementary data to this article can be found online at https://doi.org/10.1016/j.jsg.2022.104709.

References

Anderson, J.L., Smith, D.R., 1995. The effects of temperature and fO2 on the Al-in-hornblende barometer. Am. Mineral. 80, 549–559. https://doi.org/10.2138/am-1995-5-614.

Ashby, M.F., Verrall, R.A., 1973. Diffusion-accommodated flow and superplasticity. Acta Metall. 21, 149–163. https://doi.org/10.1016/0001-6160(73)90057-6.

Ayers, J.C., Crombie, S., Loflin, M., Miller, C.F., Luo, Y., 2013. Country rock monazite response to intrusion of the Searchlight pluton, southern Nevada. Am. J. Sci. 313, 345–394. https://doi.org/10.2475/04.2013.04.

Bachl, C.A., Miller, C.F., Miller, J.S., Faulds, J.E., 2001. Construction of a pluton: evidence from an exposed cross section of the Searchlight pluton, Eldorado Mountains, Nevada. GSA Bull 113, 1213–1228 https://doi.org/10.1130/0016-7606(2001)113<1213:COAPEF>2.0.CO;2.

Bachmann, F., Hielscher, R., Schaeben, H., 2010. Texture Analysis with MTEX – Free and Open Source Software Toolbox [WWW Document]. Solid State Phenom. https://doi.org/10.4028/www.scientific.net/SSP.160.63.

Behr, W.M., Platt, J.P., 2011. A naturally constrained stress profile through the middle crust in an extensional terrane. Earth Planet Sci. Lett. 303, 181–192. https://doi.org/10.1016/j.epsl.2010.11.044.

Behr, W.M., Platt, J.P., 2014. Brittle faults are weak, yet the ductile middle crust is strong: implications for lithospheric mechanics. Geophys. Res. Lett. 41, 8067–8075. https://doi.org/10.1002/2014GL061349.

Bestmann, M., Prior, D.J., 2003. Intragranular dynamic recrystallization in naturally deformed calcite marble: diffusion accommodated grain boundary sliding as a result of subgrain rotation recrystallization. J. Struct. Geol. 25, 1597–1613. https://doi.org/10.1016/S0191-8141(03)00006-3.

Blumenfeld, P., Bouchez, J.-L., 1988. Shear criteria in granite and migmatite deformed in the magmatic and solid states. J. Struct. Geol. 10, 361–372. https://doi.org/10.1016/0191-8141(88)90014-4.

Blumenfeld, P., Mainprice, D., Bouchez, J.L., 1986. C-slip in quartz from subsolidus deformed granite. Tectonophysics 127, 97–115. https://doi.org/10.1016/0040-1951(86)90081-8.

Brace, W.F., Kohlstedt, D.L., 1980. Limits on lithospheric stress imposed by laboratory experiments. J. Geophys. Res. Solid Earth 85, 6248–6252. https://doi.org/10.1029/JB085iB11p06248.

Bürgmann, R., Dresen, G., 2008. Rheology of the lower crust and upper mantle: evidence from rock mechanics, geodesy, and field observations. Annu. Rev. Earth Planet Sci. 36, 531–567. https://doi.org/10.1146/annurev.earth.36.031207.124326.

Burov, E.B., 2011. Rheology and strength of the lithosphere. Mar. Petrol. Geol. 28, 1402–1443. https://doi.org/10.1016/j.marpetgeo.2011.05.008.

Burov, E.B., Watts, A.B., 2006. The long-term strength of continental lithosphere: "jelly sandwich" or "crème brûlée". GSA Today (Geol. Soc. Am.) 7.

Byerlee, J.D., 1968. Brittle-ductile transition in rocks. J. Geophys. Res. 1896–1977 73, 4741–4750. https://doi.org/10.1029/JB073i014p04741.

Cannat, M., 1991. Plastic deformation at an oceanic spreading ridge; a microstructural study of the Site 735 gabbros (Southwest Indian Ocean). Proc. Ocean Drill. Progr. Sci. Results 118, 399–408.

Cao, W., Lee, C.-T.A., Yang, J., Zuza, A.V., 2019. Hydrothermal circulation cools continental crust under exhumation. Earth Planet Sci. Lett. 515, 248–259. https://doi.org/10.1016/j.epsl.2019.03.029.

Chapman, A.D., Kidder, S., Saleeby, J.B., Ducea, M.N., 2010. Role of extrusion of the Rand and Sierra de Salinas schists in Late Cretaceous extension and rotation of the southern Sierra Nevada and vicinity. Tectonics 29. https://doi.org/10.1029/2009TC002597.

Chatzaras, V., Tikoff, B., Kruckenberg, S.C., Titus, S.J., Teyssier, C., Drury, M.R., 2020. Stress variations in space and time within the mantle section of an oceanic transform zone: evidence for the seismic cycle. Geology 48, 569–573. https://doi.org/10.1130/G47137.1.

Claiborne, L.L., Miller, C.F., Walker, B.A., Wooden, J.L., Mazdab, F.K., Bea, F., 2006. Tracking magmatic processes through Zr/Hf ratios in rocks and Hf and Ti zoning in zircons: an example from the Spirit Mountain batholith, Nevada. Mineral. Mag. 70, 517–543. https://doi.org/10.1180/0026461067050348.

Claiborne, L.L., Miller, C.F., Wooden, J.L., 2010. Trace element composition of igneous zircon: a thermal and compositional record of the accumulation and evolution of a large silicic batholith, Spirit Mountain, Nevada. Contrib. Mineral. Petrol. 160, 511–531. https://doi.org/10.1007/s00410-010-0491-5.

Clark, M.K., Royden, L.H., 2000. Topographic ooze: building the eastern margin of Tibet by lower crustal flow. Geology 28, 703–706 https://doi.org/10.1130/0091-7613(2000)28<703:TOBTEM>2.0.CO;2.

Cross, A.J., Prior, D.J., Stipp, M., Kidder, S., 2017. The recrystallized grain size piezometer for quartz: an EBSD-based calibration. Geophys. Res. Lett. 44, 6667–6674. https://doi.org/10.1002/2017GL073836.

Davis, G.A., Lister, G.S., 1988. Detachment Faulting in Continental Extension; Perspectives from the Southwestern U.S. Cordillera. https://doi.org/10.1130/SPE218-p133.

De Bresser, J.H.P.D., Peach, C.J., Reijs, J.P.J., Spiers, C.J., 1998. On dynamic recrystallization during solid state flow: effects of stress and temperature. Geophys. Res. Lett. 25, 3457–3460. https://doi.org/10.1029/98GL02690.

Dong, Y., Cao, S., Cheng, X., Liu, J., Cao, H., 2019. Grain-size reduction of feldspar and flow of deformed granites within the Gaoligong shear zone, southwestern Yunnan, China. Sci. China Earth Sci. 62, 1379–1398. https://doi.org/10.1007/s11430-018-9351-8.

Eddy, M.P., Pamukçu, A., Schoene, B., Steiner-Leach, T., Bell, E.A., 2022. Constraints on the timescales and processes that led to high-SiO2 rhyolite production in the Searchlight pluton, Nevada, USA. Geosphere 18, 1000–1019. https://doi.org/10.1130/GES02439.1.

Etheridge, M.A., 1983. Differential stress magnitudes during regional deformation and metamorphism: upper bound imposed by tensile fracturing. Geology 11, 231–234 https://doi.org/10.1130/0091-7613(1983)11<231:DSMDRD>2.0.CO;2.

Etheridge, M.A., Wall, V.J., Cox, S.F., Vernon, R.H., 1984. High fluid pressures during regional metamorphism and deformation: implications for mass transport and deformation mechanisms. J. Geophys. Res. Solid Earth 89, 4344–4358. https://doi.org/10.1029/JB089iB06p04344.

Fagereng, Å., Biggs, J., 2019. New perspectives on 'geological strain rates' calculated from both naturally deformed and actively deforming rocks. J. Struct. Geol., Back to the future 125, 100–110. https://doi.org/10.1016/j.jsg.2018.10.004.

Faleiros, F.M., Campanha, G.A. da C., Bello, R.M. da S., Fuzikawa, K., 2010. Quartz recrystallization regimes, c-axis texture transitions and fluid inclusion reequilibration in a prograde greenschist to amphibolite facies mylonite zone (Ribeira Shear Zone, SE Brazil). Tectonophysics 485, 193–214. https://doi.org/10.1016/j.tecto.2009.12.014.

Falkner, C.M., Miller, C.F., Wooden, J.L., Heizler, M.T., 1995. Petrogenesis and tectonic significance of the calc-alkaline, bimodal Aztec Wash pluton, Eldorado Mountains, Colorado River extensional corridor. J. Geophys. Res. Solid Earth 100, 10453–10476. https://doi.org/10.1029/94JB03357.

Faulds, J.E., Feuerbach, D.L., Miller, C.F., Smith, E.I., 2001. Cenozoic Evolution of the Northern Colorado River Extensional Corridor, pp. 239–271. Southern Nevada and Northwest Arizona.

Faulds, J.E., Bell, J.W., Olson, E.L., Chaney, R.L., 2002a. Geologic map of the Nelson SW quadrangle, Clark county, Nevada. Nev. Bur. Mines Geol. Map 134.

Faulds, J.E., Olson, E.L., Harlan, S.S., McIntosh, W.C., 2002b. Miocene extension and fault-related folding in the Highland Range, southern Nevada: a three-dimensional perspective. J. Struct. Geol. 24, 861–886. https://doi.org/10.1016/S0191-8141(01)00116-X.

Faulds, J.E., Ramelli, A.R., Castor, S.B., 2010. Preliminary Geologic Map of the Searchlight Quadrangle. Clark County, Nevada.

Flowers, R.M., Farley, K.A., Ketcham, R.A., 2015. A reporting protocol for thermochronologic modeling illustrated with data from the Grand Canyon. Earth Planet Sci. Lett. 432, 425–435. https://doi.org/10.1016/j.epsl.2015.09.053.

Fukuda, J., Okudaira, T., Satsukawa, T., Michibayashi, K., 2012. Solution–precipitation of K-feldspar in deformed granitoids and its relationship to the distribution of water. Tectonophysics 532– 535, 175–185. https://doi.org/10.1016/j.tecto.2012.01.033.

Gans, P.B., Bohrson, W.A., 1998. Suppression of volcanism during rapid extension in the Basin and range Province, United States. Science 279, 66–68. https://doi.org/10.1126/science.279.5347.66.

Gans, P.B., Gentry, B.J., 2016. Dike emplacement, footwall rotation, and the transition from magmatic to tectonic extension in the Whipple Mountains metamorphic core complex, southeastern California. Tectonics 35, 2564–2608. https://doi.org/10.1002/2016TC004215.

Gottardi, R., Hughes, B., 2022. Role of fluids on deformation in mid-crustal shear zones, Raft River Mountains, Utah. Geol. Mag. 1–13 https://doi.org/10.1017/S0016756822000231.

Guenthner, W.R., Reiners, P.W., Ketcham, R.A., Nasdala, L., Giester, G., 2013. Helium diffusion in natural zircon: radiation damage, anisotropy, and the interpretation of zircon (U-Th)/He thermochronology. Am. J. Sci. 313, 145–198. https://doi.org/10.2475/03.2013.01.

Gueydan, F., Leroy, Y.M., Jolivet, L., Agard, P., 2003. Analysis of continental midcrustal strain localization induced by microfracturing and reaction-softening. J. Geophys. Res. Solid Earth 108. https://doi.org/10.1029/2001JB000611.

Harper, B.E., Miller, C.F., Koteas, G.C., Cates, N.L., Wiebe, R.A., Lazzareschi, D.S., Cribb, J.W., 2004. Granites, dynamic magma chamber processes and pluton construction: the Aztec Wash pluton, Eldorado Mountains, Nevada, USA. Earth Environ. Sci. Trans. R. Soc. Edinb. 95, 277–295. https://doi.org/10.1017/S0263593300001073.

Hauksson, E., Meier, M.-A., 2019. Applying depth distribution of seismicity to determine thermo-mechanical properties of the seismogenic crust in southern California: comparing lithotectonic blocks. Pure Appl. Geophys. 176, 1061–1081. https://doi.org/10.1007/s00024-018-1981-z.

Hinz, N.H., Faulds, Ramelli, A.R., 2012. Preliminary geologic map of the Ireteba peaks quadrangle, Clark county, Nevada. Nev. Bur. Mines Geol. Open-File Rep, 2012-09.

Hirth, G., Kohlstedt, D.L., 1996. Water in the oceanic upper mantle: implications for rheology, melt extraction and the evolution of the lithosphere. Earth Planet Sci. Lett. 144, 93–108. https://doi.org/10.1016/0012-821X(96)00154-9.

Hirth, G., Tullis, J., 1992. Dislocation creep regimes in quartz aggregates. J. Struct. Geol. 14, 145–159. https://doi.org/10.1016/0191-8141(92)90053-Y.

Jessell, M.W., 1987. Grain-boundary migration microstructures in a naturally deformed quartzite. J. Struct. Geol. 9, 1007–1014. https://doi.org/10.1016/0191-8141(87)90008-3.

Jiang, Z., Prior, D.J., Wheeler, J., 2000. Albite crystallographic preferred orientation and grain misorientation distribution in a low-grade mylonite: implications for granular flow. J. Struct. Geol. 22, 1663–1674. https://doi.org/10.1016/S0191-8141(00)00079-1.

Johnson, B., 2014. Thermal and Compositional Evolution of the Mid-miocene Searchlight Magmatic System (Nevada, USA) as Recorded in Zircon - ProQuest.

Kapp, J.D., Miller, C.F., Miller, J.S., 2002. Ireteba pluton, Eldorado Mountains, Nevada: late, deep-source, peraluminous magmatism in the cordilleran interior. J. Geol. 110, 649–669. https://doi.org/10.1086/342864.

Kenkmann, T., Dresen, G., 2002. Dislocation microstructure and phase distribution in a lower crustal shear zone – an example from the Ivrea-Zone, Italy. Int. J. Earth Sci. 91, 445–458. https://doi.org/10.1007/s00531-001-0236-9.

Ketcham, R.A., 2005. Forward and inverse modeling of low-temperature thermochronometry data. Rev. Mineral. Geochem. 58, 275–314. https://doi.org/10.2138/rmg.2005.58.11.

Kidder, S., Avouac, J., Chan, Y., 2012. Constraints from Rocks in the Taiwan Orogen on Crustal Stress Levels and Rheology.

Kilian, R., Heilbronner, R., Stünitz, H., 2011. Quartz grain size reduction in a granitoid rock and the transition from dislocation to diffusion creep. J. Struct. Geol. 33, 1265–1284. https://doi.org/10.1016/j.jsg.2011.05.004.

Kruhl, J.H., Vernon, R.H., 2005. Syndeformational emplacement of a tonalitic sheet-complex in a Late-Variscan thrust regime: fabrics and mechanism of intrusion, Monte'e Senes, Northeastern Sardinia, Italy. Can. Mineral. 43, 387–407. https://doi.org/10.2113/gscanmin.43.1.387.

Kruse, R., Stünitz, H., Kunze, K., 2001. Dynamic recrystallization processes in plagioclase porphyroclasts. J. Struct. Geol. 23, 1781–1802. https://doi.org/10.1016/S0191-8141(01)00030-X.

Kusznir, N.J., Park, R.G., 1984. Intraplate lithosphere deformation and the strength of the lithosphere. Geophys. J. Int. 79, 513–538. https://doi.org/10.1111/j.1365-246X.1984.tb02238.x.

Law, R.D., 2014. Deformation thermometry based on quartz c-axis fabrics and recrystallization microstructures: a review. J. Struct. Geol. 66, 129–161. https://doi.org/10.1016/j.jsg.2014.05.023.

Lister, G.S., Davis, G.A., 1989. The origin of metamorphic core complexes and detachment faults formed during Tertiary continental extension in the northern Colorado River region. U.S.A. J. Struct. Geol. 11, 65–94. https://doi.org/10.1016/0191-8141(89)90036-9.

Lloyd, G.E., Freeman, B., 1994. Dynamic recrystallization of quartz under greenschist conditions. J. Struct. Geol. 16, 867–881. https://doi.org/10.1016/0191-8141(94)90151-1.

Mainprice, D., Bouchez, J.-L., Blumenfeld, P., Tubià, J.M., 1986. Dominant c slip in naturally deformed quartz: implications for dramatic plastic softening at high temperature. Geology 14, 819–822 https://doi.org/10.1130/0091-7613(1986)14<819:DCSIND>2.0.CO;2.

Mainprice, D., Bachmann, F., Hielscher, R., Schaeben, H., 2015. Descriptive tools for the analysis of texture projects with large datasets using MTEX: strength, symmetry and components. Geol. Soc. Lond. Spec. Publ. 409, 251–271. https://doi.org/10.1144/SP409.8.

Mancktelow, N.S., Pennacchioni, G., 2004. The influence of grain boundary fluids on the microstructure of quartz-feldspar mylonites. J. Struct. Geol. 26, 47–69. https://doi.org/10.1016/S0191-8141(03)00081-6.

Marti, S., Stünitz, H., Heilbronner, R., Plümper, O., Kilian, R., 2018. Syn-kinematic hydration reactions, grain size reduction, and dissolution–precipitation creep in experimentally deformed plagioclase–pyroxene mixtures. Solid Earth 9, 985–1009. https://doi.org/10.5194/se-9-985-2018.

Mehl, L., Hirth, G., 2008. Plagioclase preferred orientation in layered mylonites: evaluation of flow laws for the lower crust. J. Geophys. Res. 113, B05202 https://doi.org/10.1029/2007JB005075.

Menegon, L., Pennacchioni, G., Heilbronner, R., Pittarello, L., 2008. Evolution of quartz microstructure and c-axis crystallographic preferred orientation within ductilely deformed granitoids (Arolla unit, Western Alps). J. Struct. Geol. 30, 1332–1347. https://doi.org/10.1016/j.jsg.2008.07.007.

Menegon, L., Stünitz, H., Nasipuri, P., Heilbronner, R., Svahnberg, H., 2013. Transition from fracturing to viscous flow in granulite facies perthitic feldspar (Lofoten, Norway). J. Struct. Geol. 48, 95–112. https://doi.org/10.1016/j.jsg.2012.12.004.

Miller, C.F., Bradfish, L.J., 1980. An inner Cordilleran belt of muscovite-bearing plutons. Geology 8 (9), 412–416. https://doi.org/10.1130/0091-7613(1980)8<412:AICBOM>2.0.CO;2.

Miller, J., Miller, C.F., Wooden, J.L., Perrault, D., Hodge, K., et al., 2006. 2 Million Year History of Plutonism and Volcanism in the Searchlight Magma System, Eldorado Mountains, Nevada (USA). Presented at the American Geophysical Union conference.

Miranda, E.A., Hirth, G., John, B.E., 2016. Microstructural evidence for the transition from dislocation creep to dislocation-accommodated grain boundary sliding in naturally deformed plagioclase. J. Struct. Geol. 92, 30–45. https://doi.org/10.1016/j.jsg.2016.09.002.

Montési, L.G.J., Hirth, G., 2003. Grain size evolution and the rheology of ductile shear zones: from laboratory experiments to postseismic creep. Earth Planet Sci. Lett. 211, 97–110. https://doi.org/10.1016/S0012-821X(03)00196-1.

Mutch, E.J.F., Blundy, J.D., Tattitch, B.C., Cooper, F.J., Brooker, R.A., 2016. An experimental study of amphibole stability in low-pressure granitic magmas and a revised Al-in-hornblende geobarometer. Contrib. Mineral. Petrol. 171, 85. https://doi.org/10.1007/s00410-016-1298-9.

Nazareth, J.J., Hauksson, E., 2004. The seismogenic thickness of the southern California crust. Bull. Seismol. Soc. Am. 94, 940–960. https://doi.org/10.1785/0120020129.

Negrini, M., Stünitz, H., Nasipuri, P., Menegon, L., Morales, L.F.G., 2014. Semibrittle deformation and partial melting of perthitic K-feldspar: an experimental study. J. Geophys. Res. Solid Earth 119, 3478–3502. https://doi.org/10.1002/2013JB010573.

Neumann, B., 2000. Texture development of recrystallised quartz polycrystals unravelled by orientation and misorientation characteristics. J. Struct. Geol. 22, 1695–1711. https://doi.org/10.1016/S0191-8141(00)00060-2.

Nevitt, J.M., Warren, J.M., Kidder, S., Pollard, D.D., 2017a. Comparison of thermal modeling, microstructural analysis, and Ti-in-quartz thermobarometry to constrain the thermal history of a cooling pluton during deformation in the Mount Abbot Quadrangle, CA. G-cubed 18, 1270–1297. https://doi.org/10.1002/2016GC006655.

Nevitt, J.M., Warren, J.M., Pollard, D.D., 2017b. Testing constitutive equations for brittle-ductile deformation associated with faulting in granitic rock. J. Geophys. Res. Solid Earth 122, 6269–6293. https://doi.org/10.1002/2017JB014000.

Oliot, E., Goncalves, P., Marquer, D., 2010. Role of plagioclase and reaction softening in a metagranite shear zone at mid-crustal conditions (Gotthard Massif, Swiss Central Alps). J. Metamorph. Geol. 28, 849–871. https://doi.org/10.1111/j.1525-1314.2010.00897.x.

Olsen, T.S., Kohlstedt, D.L., 1984. Analysis of dislocations in some naturally deformed plagioclase feldspars. Phys. Chem. Miner. 11, 153–160. https://doi.org/10.1007/BF00387845.

Passchier, C.W., 1982. Pseudotachylyte and the development of ultramyionite bands in the saint- barthdlerny Massif, French pyrenees. J. Struct. Geol. 4, 69–79.

Paterson, S.R., Vernon, R.H., Tobisch, O.T., 1989. A review of criteria for the identification of magmatic and tectonic foliations in granitoids. J. Struct. Geol. 11, 349–363. https://doi.org/10.1016/0191-8141(89)90074-6.

Paterson, S.R., Fowler, T.K., Schmidt, K.L., Yoshinobu, A.S., Yuan, E.S., Miller, R.B., 1998. Interpreting magmatic fabric patterns in plutons. Lithos 44, 53–82. https://doi.org/10.1016/S0024-4937(98)00022-X.

Platt, J.P., 2015. Rheology of two-phase systems: a microphysical and observational approach. J. Struct. Geol. 77, 213–227. https://doi.org/10.1016/j.jsg.2015.05.003.

Platt, J.P., Behr, W.M., 2011. Grainsize evolution in ductile shear zones: implications for strain localization and the strength of the lithosphere. J. Struct. Geol. 33, 537–550. https://doi.org/10.1016/j.jsg.2011.01.018.

Post, A., Tullis, J., 1999. A recrystallized grain size piezometer for experimentally deformed feldspar aggregates. Tectonophysics 303, 159–173. https://doi.org/10.1016/S0040-1951(98)00260-1.

Pryer, L.L., 1993. Microstructures in feldspars from a major crustal thrust zone: the Grenville Front, Ontario, Canada. J. Struct. Geol. 15, 21–36. https://doi.org/10.1016/0191-8141(93)90076-M.

Ree, J.-H., Kim, H.S., Han, R., Jung, H., 2005. Grain-size reduction of feldspars by fracturing and neocrystallization in a low-grade granitic mylonite and its rheological effect. Tectonophysics 407, 227–237. https://doi.org/10.1016/j.tecto.2005.07.010.

Reiners, P.W., Farley, K.A., Hickes, H.J., 2002. He diffusion and (U–Th)/He thermochronometry of zircon: initial results from fish canyon tuff and gold butte. Tectonophysics, low temperature thermochronology: from tectonics to. Landscape Evolution 349, 297–308. https://doi.org/10.1016/S0040-1951(02)00058-6.

Reiners, P.W., Spell, T.L., Nicolescu, S., Zanetti, K.A., 2004. Zircon (U-Th)/He thermochronometry: He diffusion and comparisons with 40Ar/39Ar dating. Geochem. Cosmochim. Acta 68, 1857–1887. https://doi.org/10.1016/j.gca.2003.10.021.

Reynolds, S.J., Lister, G.S., 1990. Folding of mylonitic zones in Cordilleran metamorphic core complexes: evidence from near the mylonitic front. Geology 18, 216–219 https://doi.org/10.1130/0091-7613(1990)018<0216:FOMZIC>2.3.CO;2.

Rodriguez-Arriaga, A., 2021. Characterization of the Deformation across a Brittle-Ductile Transition Zone: Geologic Mapping and Microstructures in the Ireteba Pluton in the Southern Basin and Range. University of Nevada, Reno, Reno, NV.

Rybacki, E., Dresen, G., 2000. Dislocation and diffusion creep of synthetic anorthite aggregates. J. Geophys. Res. Solid Earth 105, 26017–26036. https://doi.org/10.1029/2000JB900223.

Rybacki, E., Dresen, G., 2004. Deformation mechanism maps for feldspar rocks. Tectonophysics 382, 173–187. https://doi.org/10.1016/j.tecto.2004.01.006.

Schutt, D.L., Lowry, A.R., Buehler, J.S., 2018. Moho temperature and mobility of lower crust in the western United States. Geology 46, 219–222. https://doi.org/10.1130/G39507.1.

Shi, X., Kirby, E., Furlong, K.P., Meng, K., Robinson, R., Wang, E., 2015. Crustal strength in central Tibet determined from Holocene shoreline deflection around Siling Co. Earth Planet Sci. Lett. 423, 145–154. https://doi.org/10.1016/j.epsl.2015.05.002.

Sibson, R.H., 1977. Kinetic shear resistance, fluid pressures and radiation efficiency during seismic faulting. Pure Appl. Geophys. 115, 387–400. https://doi.org/10.1007/BF01637116.

Sibson, R.H., 1984. Roughness at the base of the seismogenic zone: contributing factors. J. Geophys. Res. Solid Earth 89, 5791–5799. https://doi.org/10.1029/JB089iB07p05791.

Sibson, R.H., 1986. Earthquakes and Rock Deformation in Crustal Fault Zones 28.

Simpson, C., Wintsch, R.P., 1989. Evidence for deformation-induced K-feldspar replacement by myrmekite. J. Metamorph. Geol. 7, 261–275. https://doi.org/10.1111/j.1525-1314.1989.tb00588.x.

Singleton, J.S., Mosher, S., 2012. Mylonitization in the lower plate of the Buckskin-Rawhide detachment fault, west-central Arizona: implications for the geometric evolution of metamorphic core complexes. J. Struct. Geol. 39, 180–198. https://doi.org/10.1016/j.jsg.2012.02.013.

Singleton, J.S., Seymour, N.M., Reynolds, S.J., Vomocil, T., Wong, M.S., 2019. Distributed Neogene faulting across the western to central Arizona metamorphic core complex belt: synextensional constriction and superposition of the Pacific–North America plate boundary on the southern Basin and Range. Geosphere 15, 1409–1435. https://doi.org/10.1130/GES02036.1.

Skemer, P., Katayama, I., Jiang, Z., Karato, S., 2005. The misorientation index: development of a new method for calculating the strength of lattice-preferred orientation. Tectonophysics 411, 157–167. https://doi.org/10.1016/j.tecto.2005.08.023.

Speciale, P.A., Tokle, L., Behr, W.M., 2022. Feldspar and orthopyroxene piezometers constrained using quartz–feldspar and olivine–orthopyroxene mineral pairs from natural mylonites. J. Struct. Geol. 154, 104495 https://doi.org/10.1016/j.jsg.2021.104495.

Spencer, J.E., Singleton, J.S., Strickland, E., Reynolds, S.J., Love, D., Foster, D.A., Johnson, R., 2018. Geodynamics of Cenozoic extension along a transect across the Colorado River extensional corridor, southwestern USA. Lithosphere 10, 743–759. https://doi.org/10.1130/L1002.1.

Stipp, M., Stünitz, H., Heilbronner, R., Schmid, S.M., 2002. Dynamic recrystallization of quartz: correlation between natural and experimental conditions. Geol. Soc. Lond. Spec. Publ. 200, 171–190. https://doi.org/10.1144/GSL.SP.2001.200.01.11.

Strickland, E.D., Singleton, J.S., Haxel, G.B., 2018. Orocopia Schist in the northern Plomosa Mountains, west-central Arizona: a Laramide subduction complex exhumed in a Miocene metamorphic core complex. Lithosphere 10, 723–742. https://doi.org/10.1130/L742.1.

Stünitz, H., Fitz Gerald, J.D.F., 1993. Deformation of granitoids at low metamorphic grade. II: granular flow in albite-rich mylonites. Tectonophysics 221, 299–324. https://doi.org/10.1016/0040-1951(93)90164-F.

Sullivan, W.A., Boyd, A.S., Monz, M.E., 2013. Strain localization in homogeneous granite near the brittle–ductile transition: a case study of the Kellyland fault zone, Maine, USA. J. Struct. Geol. 56, 70–88. https://doi.org/10.1016/j.jsg.2013.09.003.

Svahnberg, H., Piazolo, S., 2010. The initiation of strain localisation in plagioclase-rich rocks: insights from detailed microstructural analyses. J. Struct. Geol. 32, 1404–1416. https://doi.org/10.1016/j.jsg.2010.06.011.

Thigpen, J.R., Law, R.D., Lloyd, G.E., Brown, S.J., 2010. Deformation temperatures, vorticity of flow, and strain in the Moine thrust zone and Moine nappe: reassessing the tectonic evolution of the Scandian foreland–hinterland transition zone. J. Struct. Geol. 32, 920–940. https://doi.org/10.1016/j.jsg.2010.05.001.

Tsurumi, J., Hosonuma, H., Kanagawa, K., 2003. Strain localization due to a positive feedback of deformation and myrmekite-forming reaction in granite and aplite mylonites along the Hatagawa Shear Zone of NE Japan. J. Struct. Geol. 25, 557–574. https://doi.org/10.1016/S0191-8141(02)00048-2.

Tullis, J., Yund, R.A., 1985. Dynamic recrystallization of feldspar: a mechanism for ductile shear zone formation. Geology 13, 238–241 https://doi.org/10.1130/0091-7613(1985)13<238:DROFAM>2.0.CO;2.

Tullis, J., Yund, R.A., 1987. Transition from cataclastic flow to dislocation creep of feldspar: mechanisms and microstructures. Geology 15, 606–609 https://doi.org/10.1130/0091-7613(1987)15<606:TFCFTD>2.0.CO;2.

Tullis, J., Yund, R.A., 1991. Diffusion creep in feldspar aggregates: experimental evidence. J. Struct. Geol. 13, 987–1000. https://doi.org/10.1016/0191-8141(91)90051-J.

Urai, J.L., Means, W.D., Lister, G.S., 1986. Dynamic recrystallization of minerals. In: Mineral and Rock Deformation. American Geophysical Union (AGU), pp. 161–199. https://doi.org/10.1029/GM036p0161.

Viegas, G., Menegon, L., Archanjo, C., 2016. Brittle grain-size reduction of feldspar, phase mixing and strain localization in granitoids at mid-crustal conditions (Pernambuco shear zone, NE Brazil). Solid Earth 7, 375–396. https://doi.org/10.5194/se-7-375-2016.

Vollmer, F.W., 1990. An application of eigenvalue methods to structural domain analysis. GSA Bull 102, 786–791 https://doi.org/10.1130/0016-7606(1990)102<0786:AAOEMT>2.3.CO;2.

Walker, B.A., Miller, C.F., Lowery Claiborne, L., Wooden, J.L., Miller, J.S., 2007. Geology and geochronology of the Spirit Mountain batholith, southern Nevada: implications for timescales and physical processes of batholith construction. J. Volcanol. Geotherm. Res., Large Silicic Magma Systems 167, 239–262. https://doi.org/10.1016/j.jvolgeores.2006.12.008.

Warren, J.M., Hirth, G., 2006. Grain size sensitive deformation mechanisms in naturally deformed peridotites. Earth Planet Sci. Lett. 248, 438–450. https://doi.org/10.1016/j.epsl.2006.06.006.

Watts, A.B., Burov, E.B., 2003. Lithospheric strength and its relationship to the elastic and seismogenic layer thickness. Earth Planet Sci. Lett. 213, 113–131. https://doi.org/10.1016/S0012-821X(03)00289-9.

White, S., 1977. Geological significance of recovery and recrystallization processes in quartz. Tectonophysics, Fabrics, microstructures, and microtectonics 39, 143–170. https://doi.org/10.1016/0040-1951(77)90093-2.

White, S., 1979. Grain and sub-grain size variations across a mylonite zone. Contrib. Mineral. Petrol. 70, 193–202. https://doi.org/10.1007/BF00374448.

Wintsch, R.P., Yi, K., 2002. Dissolution and replacement creep: a significant deformation mechanism in mid-crustal rocks. J. Struct. Geol., Micro structural Processes: A Special Issue in Honor of the Career Contributions of R.H. Vernon 24, 1179–1193. https://doi.org/10.1016/S0191-8141(01)00100-6.

Wolfe, M.R., Stockli, D.F., 2010. Zircon (U–Th)/He thermochronometry in the KTB drill hole, Germany, and its implications for bulk He diffusion kinetics in zircon. Earth Planet Sci. Lett. 295, 69–82. https://doi.org/10.1016/j.epsl.2010.03.025.

Xiao, X., Wirth, R., Dresen, G., 2002. Diffusion creep of anorthite-quartz aggregates. J. Geophys. Res. Solid Earth 107. https://doi.org/10.1029/2001JB000789. ECV 6-1-ECV 6-15.

Zhao, B., Bürgmann, R., Wang, D., Tan, K., Du, R., Zhang, R., 2017. Dominant controls of downdip afterslip and viscous relaxation on the postseismic displacements following the Mw7.9 gorkha, Nepal, earthquake. J. Geophys. Res. Solid Earth 122, 8376–8401. https://doi.org/10.1002/2017JB014366.

Zuza, A.V., Cao, W., 2020. Seismogenic thickness of California: implications for thermal structure and seismic hazard. Tectonophysics 782– 783, 228426 https://doi.org/10.1016/j.tecto.2020.228426.

Zuza, A.V., Cao, W., Hinz, N.H., DesOrmeau, J.W., Odlum, M.L., Stockli, D.F., 2019. Footwall rotation in a regional detachment fault system: evidence for horizontal-Axis rotational flow in the Miocene Searchlight pluton. NV. Tectonics 38, 2506–2539. https://doi.org/10.1029/2019TC005513.

Zuza, A.V., Levy, D.A., Mulligan, S.R., 2022a. Geologic field evidence for non-lithostatic overpressure recorded in the North American Cordillera hinterland, northeast Nevada - ScienceDirect. Geosci. Front. 13.

Zuza, A.V., Levy, D.A., Dee, S., DesOrmeau, J.W., Cheng, F., Li, X., 2022b. Structural architecture and attenuation of the ductile lower plate of the Ruby Mountain-East Humboldt Range metamorphic core complex, northeast Nevada. Tectonics. https://doi.org/10.1029/2021TC007162.